



OPEN ACCESS

EDITED BY

Robert Bowell,
SRK Consulting UK, United Kingdom

REVIEWED BY

Tong Hou,
China University of Geosciences, China
Hua-Wen Cao,
Chengdu University of Technology, China

*CORRESPONDENCE

Jianguo Wang,
✉ lywjg467047@126.com

RECEIVED 19 April 2024

ACCEPTED 10 September 2024

PUBLISHED 19 September 2024

CITATION

Li Y, Wang J, Yu Z, Wei S, Ren H, Ma M,
Wang Z and Hu J (2024) Ore genesis of the
Chazangcuo Cu-Pb-Zn deposit in Tibet:
evidence from mineralogy, fluid inclusions,
S-Pb isotopes, and elemental geochemistry.
Front. Earth Sci. 12:1420043.
doi: 10.3389/feart.2024.1420043

COPYRIGHT

© 2024 Li, Wang, Yu, Wei, Ren, Ma, Wang and
Hu. This is an open-access article distributed
under the terms of the [Creative Commons
Attribution License \(CC BY\)](https://creativecommons.org/licenses/by/4.0/). The use,
distribution or reproduction in other forums is
permitted, provided the original author(s) and
the copyright owner(s) are credited and that
the original publication in this journal is cited,
in accordance with accepted academic
practice. No use, distribution or reproduction
is permitted which does not comply with
these terms.

Ore genesis of the Chazangcuo Cu-Pb-Zn deposit in Tibet: evidence from mineralogy, fluid inclusions, S-Pb isotopes, and elemental geochemistry

Yan Li¹, Jianguo Wang^{1,2*}, Zezhang Yu³, Shengyun Wei¹,
Haidong Ren¹, Ming Ma¹, Zhinan Wang¹ and Jian Hu¹

¹School of Geological Engineering, Qinghai University, Xining, China, ²Key Laboratory of Cenozoic Resources and Environment in Northern Margin of the Tibetan Plateau, Xining, China, ³Tibet Xinhu Mining Company Limited, Lhasa, China

The Chazangcuo copper-lead-zinc deposit (hereafter referred to as the Chazangcuo deposit) is situated in the northern portion of the western section of the Gangdese polymetallic metallogenic belt in Tibet, with ore bodies strictly governed by Linzizong Group magmatic rocks and EW-trending faults. This study aims to ascertain the mineralization periods, sources of ore-forming materials, metallogenic physicochemical conditions, and genesis of this deposit. Based on comprehensive field geological surveys, sampling, and microscopic examination of petrological and mineralogical characteristics, we perform qualitative and quantitative geochemical analyses of major elements, trace elements, and rare earth elements (REEs), fluid inclusions, and sulfur and lead isotopes. The findings reveal that the mineralization process of the Chazangcuo deposit can be divided into three periods and four stages: the magmatic-hydrothermal, hydrothermal, and supergene mineralization periods sequentially, which consist of the mineralization stages of quartz-pyrite-sphalerite, medium-low-temperature hydrothermal sulfides, chlorite-carbonate minerals, and supergene oxidation in a chronological order. The ore-forming fluids prove to be medium-low-temperature low-density fluids, and the ore-forming materials are characteristic of upper crustal-derived materials. The ore-forming environment is a medium-low mineralization temperature, a shallow and weakly reducing environment. Overall, the Chazangcuo deposit is identified as a medium-low-temperature magmatic-hydrothermal deposit. The metallogenic model has the vertical zoning characteristics of lead-zinc in the upper part and copper in the lower part.

KEYWORDS

fluid inclusion, S-Pb isotopes, electron probe, mineralization periods, source of metallogenic materials, ore genesis

1 Introduction

The Qinghai-Tibet Plateau, an integral part of the Tethyan-Himalayan metallogenic domain, stands out as both the most significant region with extensive polymetallic

mineralization of China and a globally recognized polymetallic metallogenic province (Hou et al., 2006a; Song et al., 2014; Tang, 2019; Wang et al., 2020; Li et al., 2021). This region has experienced a series of geological transformations, including the breakup of the Pangea supercontinent and the cracking of the Tethys Ocean during the Paleozoic, followed by Mesozoic accretionary orogeny and Cenozoic continental collision. These events sparked orogenesis including intense crust-mantle interactions, intense magma-fluid activity, and active vertical growth and lateral accretion of the crust, governing the formation and development of giant metallogenic systems. Many researchers assert that collisional orogenic processes led to significant geological changes, such as crustal thickening and shortening, lithospheric shear, and mantle thinning, potentially triggering multi-episodic large-scale metallogenic events and leading to the formation of giant metallogenic systems. Concurrently, ongoing geological activity further caused the superimposed modification of numerous pre-existing deposits, creating a distinctive superimposed giant metallogenic system (Hou et al., 2012; He et al., 2023; Liang et al., 2023; Wang et al., 2024).

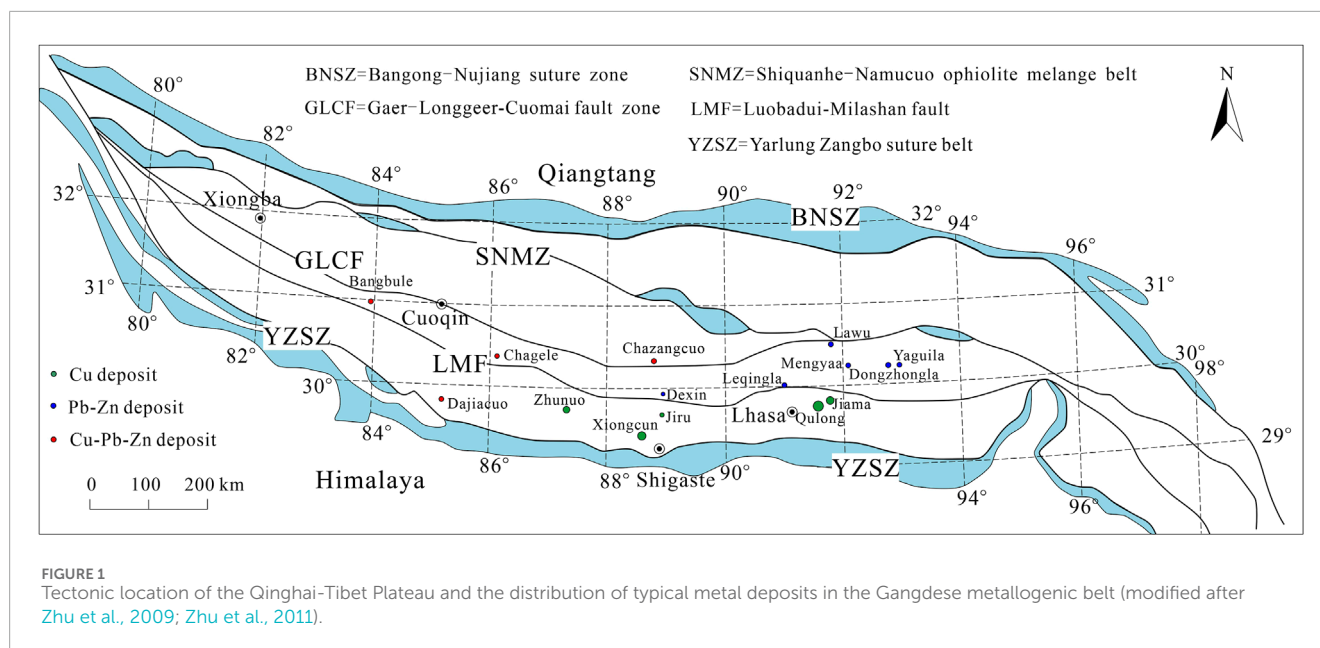
In recent years, based on extensive field surveys, experiments, and theoretical research, some researchers have linked the evolution of large-scale metallogenic phenomena in the Gangdese metallogenic belt closely with the Cenozoic-Mesozoic transition from oceanic to continental environments and the continental convergence throughout the geological history. These led to the Mesozoic mineralization of convergent continental margins, Paleogene continental collision, and the formation of an extensional metallogenic system during the Neogene's post-collision period. Consequently, porphyry-skarn-type polymetallic belts, exemplified by Qulong and Jiama, and skarn-hydrothermal vein-type lead-zinc belts, represented by Dongzhongla, Narusongduo, and Mengyaa, were formed, epitomizing typical deposit associations in a porphyry metallogenic system (Fei et al., 2011; Wang et al., 2014; Fu et al., 2015; Gong et al., 2022; Wu et al., 2023). Research also shows that epithermal deposits frequently occur in the upper and peripheral areas of porphyry metallogenic systems, indicating that both deposit types share close connections in terms of material sources, spatiotemporal distribution, tectonic styles, fluid characteristic evolution, and the precipitation mechanisms of mineralized elements (Xu et al., 2022; Xiong et al., 2022). Although the copper-lead-zinc polymetallic belt in the northern part of the Gangdese's western section has great metallogenic prospects, current research on its deposit types and genetic mechanisms remains somewhat limited. At present, the research on the Chazangcuo Cu-Pb-Zn deposit is limited to the geological characteristics of the deposit, ore-forming fluid, and material sources. The ore-forming fluid mainly comes from magmatic-hydrothermal fluid in the early stage, and the ore-forming fluid has the characteristics of mixed fluid due to the continuous addition of atmospheric precipitation in the later stage. The ore-forming materials mainly come from the magmatic source of the upper crust (Jiang et al., 2015; Gao, 2015); in addition, there is some controversy about the ore-bearing strata of the Chazangcuo Cu-Pb-Zn deposit. Some scholars believe that the ore-bearing strata are the andesite of the Dianzhong Formation of the Linzizong Group (Jiang et al., 2015), and some scholars believe that the ore-bearing strata are the Miocene Wuyu Group volcanic rocks (Gao, 2015); moreover, there is still a lack

of unified understanding of the metallogenic period, metallogenic physical and chemical conditions and metallogenic model of the deposit. For instance, the Chazangcuo deposit's tectonic-magmatic evolution resembles that of other lead-zinc deposits in the copper-lead-zinc polymetallic belt; however, questions whether they share similar metallogenic periods, metallogenic physical and chemical conditions and metallogenic model remain unsolved. Therefore, based on previous research, this study investigates the geological, petrological, and mineralogical characteristics of the Chazangcuo deposit, involving the geochemical analyses of major elements, trace elements, and REEs, fluid inclusions, and sulfur and lead isotopes and the electron probe microanalysis of polymetallic sulfides. This study further elucidates the Chazangcuo deposit's ore-bearing strata and the metallogenic geological environment including metallogenic temperature and pressure and delves into the mineralization periods, sources of ore-forming materials, and metallogenic physicochemical conditions, systematically clarifying the genesis and type of the deposit. This study aims to provide a theoretical and practical foundation for summarizing metallogenic regularities, indicating prospecting targets, and planning exploration activities in the Gangdese's western section.

2 Regional geological setting

The study area is positioned on the Gangdese-Nyainqentanglha plate, forming part of the northern subsection of the Gangdese metallogenic belt. It is nestled between the Bangonghu-Nujiang and Yarlung Zangbo suture zones, extending in an EW direction. The Gangdese metallogenic belt is known for hosting distinct porphyry copper deposits such as Qulong, Xiongcuo, Zhunuo, and Jiama, notable lead-zinc deposits like Dexin, Dongzhongla, Mengyaa, and Lawu, and copper-lead-zinc deposits including Chagele and Chazangcuo (Yao et al., 2014; Fu et al., 2015; Ke et al., 2017; Dai et al., 2018; Ling et al., 2021; Xie et al., 2022; Figure 1).

Paleozoic, Mesozoic, and Cenozoic strata are exposed in the study area, from the base upwards, consisting of Carboniferous Yongzhu ($C_{1-2}y$) and Laga ($(C_2-P_1)l$) formations, the Permian Angjie Formation (P_1a), the Paleocene Dianzhong ($(K_2-E_1)d$), Nianbo (E_2n), and Pana (E_2p) formations, the Neogene Wuyu Group (N_2wy^2), and the Quaternary (Q). The Carboniferous Yongzhu ($C_{1-2}y$) and Laga ($(C_2-P_1)l$) formations comprise grayish-green fine-grained sandstones intercalated with medium-fine-grained quartz sandstones. The Permian Angjie Formation (P_1a) encompasses pebbled sandstones and sandstones interspersed with thin-bedded limestones. The Paleocene Dianzhong Formation ($(K_2-E_1)d$) is made up of andesites and dacites mingled with a minor quantity of tuffaceous sandstones, the Nianbo Formation (E_2n) consists of tuffaceous conglomerates and sandstones interlaid with siltstones and scant tuffs, and the Pana Formation (E_2p) is composed of andesites, basalts, and dacites interspersed with dacitic volcanoclastic rocks. The Neogene Wuyu Group (N_2wy^2) consists of gray and grayish-purple intermediate-acidic volcanic rocks intercalated with volcanoclastic rocks, and the Quaternary (Q) comprises alluvial and lacustrine sediments. The study area's structural framework is composed predominantly of nearly EW-oriented folds, thrust fault zones, and nearly SN-trending tensional fault zones, with well-developed fault structures mainly striking NWW, NE, and nearly



EW (Li et al., 2005). Magmatic rocks are extensively distributed in the nearly EW direction in the study area, markedly influenced by fault structures. They exhibit a prominent presence of the volcanic rock sections of the Neogene Wuyu Group, the volcanic rocks of the Paleogene Linzizong Group, and the intermediate-acid intrusions of the Late Cretaceous, with the latter primarily including black mica granites, granite porphyries, and granite diorite porphyries (Figure 2A).

3 Geological characteristics of the Chazangcuo deposit

The exposed strata within the Chazangcuo deposit encompass the Dianzhong Formation of the Paleogene Linzizong Group, the volcanic rock section of the Neogene Wuyu Group, and the Quaternary. The Dianzhong Formation primarily exhibits andesites, whereas the Wuyu Group volcanic section is chiefly composed of dacites and tuffs. The Quaternary strata consist predominantly of alluvial and lacustrine sediments, with the alluvial sediments comprising gravels and sands. Surrounding the Chazangcuo deposit, an extensive array of Late Cretaceous granites is developed, albeit minimally within the deposit itself. The ore-hosting surrounding rocks mainly present an island-arc volcanic rock suite (Figure 2B). The fault structure in the mining area is very developed, primarily in the EW-NW trending, with the phenomenon of cutting ore body, which is the ore-controlling, ore-bearing and ore-conducting structure (Jiang et al., 2015; Figure 2C).

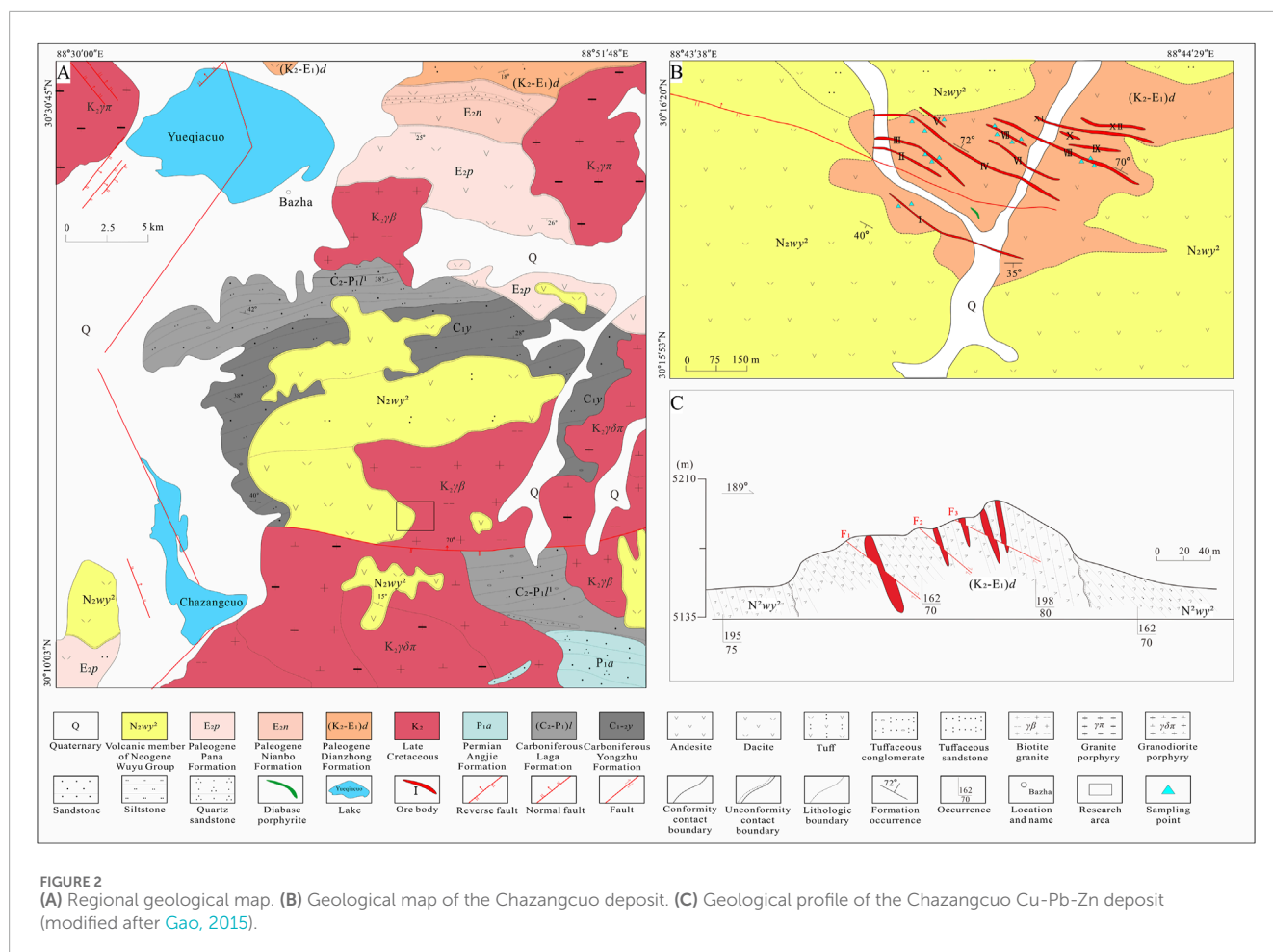
Within the Chazangcuo deposit, 12 copper-lead-zinc ore bodies are identified, all distributed within volcanic rocks' fault structures as veins. Veins in the deposit include copper-lead-zinc, quartz, chlorite, and carbonate mineral veins. The ores in the deposit feature high grades, with dominant metal minerals primarily including chalcocopyrite, sphalerite, galena, and pyrite (Figures 3A–C). Of these, the chalcocopyrite manifests as

idiomorphic-hypidiomorphic granules, sized between 0.02 and 9.00 mm, interspersed among gangue minerals. The sphalerite and galena are xenomorphic granular, with sizes ranging from 0.10 to 1.10 mm and 0.01–0.60 mm, respectively, while the pyrite is hypidiomorphic granular, approximately 0.16 mm in size. The ore mineral assemblages primarily include quartz-pyrite-sphalerite-galena, chalcocopyrite-pyrite-galena, chalcocopyrite-galena-sphalerite, and quartz-pyrite-sphalerite. The non-metallic minerals in the deposit primarily include quartz, sericite, chlorite, and carbonate minerals (Figures 3D–F). The ore textures mainly comprise xenomorphic granular (Figure 3G), hypidiomorphic-xenomorphic granular (Figure 3H), idiomorphic-hypidiomorphic granular (Figure 3I), granular crystalloblastic (Figures 3D–F), cataclastic (Figures 3D, E), fissure filling, and dissolution metasomatic textures. The structures are predominantly massive (Figures 3D–F), clumped, streaked, disseminated (Figures 3G–I), and stockwork-like. Alterations such as silicification, pyrite, zoisite, sericite, clay, and chlorite alterations are prevalent within the Chazangcuo deposit (Figures 3D–F).

4 Sampling and analysis methods

4.1 Samples

In this study, the samples of copper, lead, and zinc ores for main and trace elements, fluid inclusions, S-Pb isotopes, and electron probes were obtained from chalcocopyrite, galena, sphalerite, and pyrite in ore-bearing British veins and ore-bearing calcite veins of Chazangcuo Cu-Pb-Zn deposit of different mineralization stages and different mineral combinations. See Figure 2B for specific sampling locations. According to field geological survey, hand sample identification, and indoor microscopic identification of mineral composition analysis, color mainly includes gray, gray-green, and white, and Chazangcuo ore grade is higher. The



mineral species of ore is relatively simple. The main metallic minerals are chalcopyrite, sphalerite, galena, and pyrite. Non-metallic minerals such as quartz, carbonate minerals, etc. The ore textures mainly comprise xenomorphic granular, hypidiomorphic-xenomorphic granular, etc. The ore structures are mainly the block structure, the secondary clumped, disseminated, and so on (Figures 3A–I).

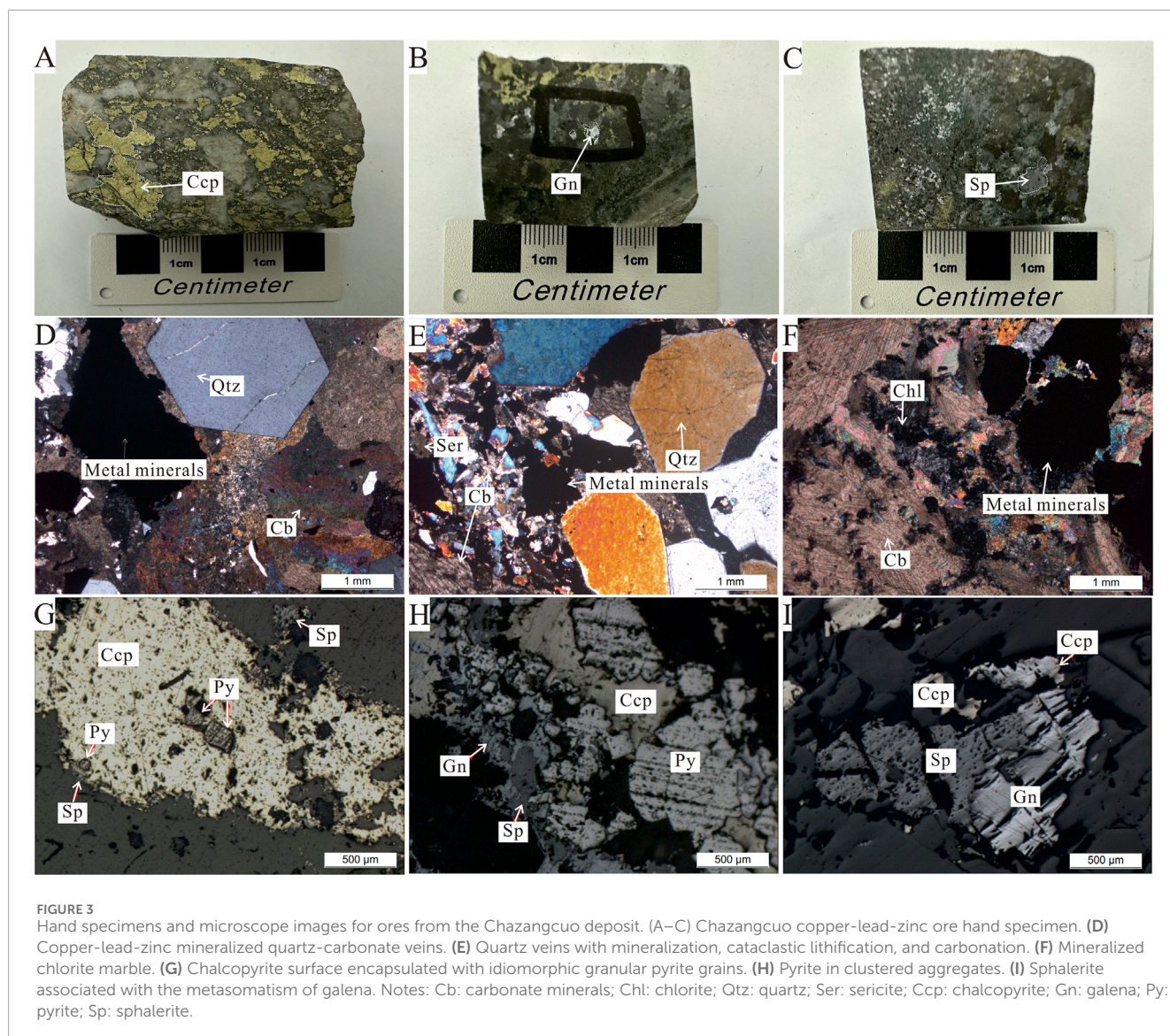
4.2 Major elements, trace elements, and REEs

The geochemical samples analyzed were all whole-rock powders, conducted at Aoshi Analysis and Testing (Guangzhou) Co., Ltd. The major elements of 15 samples were assessed using the ME-XRF15c technique in several steps: sample grinding, pre-drying, adding a lithium borate flux with sodium nitrate, thorough mixing, and high-temperature melting. The molten samples were then cast into a flat glass disk for analyses using X-ray fluorescence spectrometry, with relative errors in test results of less than 5%. The trace element and REE of 11 samples analyses were conducted using the ME-MS61r method, involving dissolving samples in perchloric, nitric, hydrofluoric, and hydrochloric acids, followed by volume fixing using dilute hydrochloric acids. Then, inductively coupled plasma-optical emission spectroscopy (ICP-ES) was employed for analysis.

In the case of too high Bi/Hg/Mo/Ag/W concentrations, dilution was required before an analysis using an inductively coupled plasma mass spectrometer. Spectral interferences between elements were corrected, with relative errors of less than 10%. For REE analysis, lithium borate (LiBO₂/Li₂B₄O₇) was added to samples, followed by thorough mixing, and melting in a furnace at 1,025°C. Once cooled, the samples were dissolved in nitric, hydrochloric, and hydrofluoric acids, processed for volume fixing, and then analyzed using a plasma mass spectrometer.

4.3 Fluid inclusions

Fluid inclusion analyses using microcalorimetry were carried out at the State Key Laboratory of Geological Processes and Mineral Resources, China University of Geosciences (Wuhan) using a Linkam THMS-600 hot and cold stage from the UK. The accuracy of temperature measurements varies with the range. Specifically, the errors were approximately 0.2°C below 31°C, around 1°C between 31°C and 300°C, and about 2°C above 300°C. Calcite and quartz veins from high-grade ores were finely ground into 0.03-mm-thick sections for microscopic examination. Selected fluid inclusions were subjected to heating and cooling to observe temperature changes. The procedure involved reducing the temperature to -80°C to freeze all fluid inclusions initially, then gradually warming to



–10°C, followed by a slow increase to 0°C at a rate of 1°C/min to accurately determine the freezing point. The temperature was then elevated at 10°C/min until bubble contraction was observed, and then the heating rate was decreased to 2°C/min to determine the homogenization temperature.

4.4 Sulfur and lead isotopes

Sulfur and lead isotope analyses were performed at the Aoshi Analysis and Testing (Guangzhou) Co., Ltd. Samples from the quartz-sulfide mineralization stage were crushed, and pure (99% or higher) monominerals such as chalcopyrite, galena, and sphalerite were selected under a binocular microscope. After ultrasonic cleaning to remove surface dust, the minerals were pulverized to 200 mesh fractions using an agate mortar. Sulfur isotope analysis was conducted using the S-ISTP01 method, with $\delta^{34}\text{S}$ values measured using a mass spectrometer coupled to an element analyzer and standardized against the Vienna-defined canyon diablo troilite

(V-CDT) standard. The detection range is 0.01%–50%, and the relative error (RE) is less than 3.5%. Lead isotopes were assessed using the Pb-IRM01 method and high-resolution inductively coupled plasma sector field mass spectrometry (HR-ICP-SFMS). The detection range is 0.001%–20%, and the relative error (RE) is less than 3.5%.

4.5 Electron probe microanalysis

Electron probe microanalysis was conducted at the State Key Laboratory of Plateau Ecology and Agriculture, Qinghai University. Using a JXA-8230 electronic probe analyzer supplied by Nihon Electronics, Inc., the chalcopyrite, pyrite, galena, and sphalerite samples from the Chazangcuo deposit were examined at 91 sites under 20 kV and 50 nA. Spot sizes were set at approximately 1 μm for standard elements and at 3 μm for volatile elements to ensure that the sizes of analyzed mineral grains were 3 μm or above.

TABLE 1 Analytical results of major elements.

Sample no.	SiO ₂	TiO ₂	Al ₂ O ₃	TFe ₂ O ₃	CuO	PbO	ZnO	MnO	MgO	CaO	Na ₂ O	K ₂ O	P ₂ O ₅	SO ₃
CZC-1	33.46	0.64	8.53	12.44	6.74	0.61	0.65	0.51	1.27	8.71	0.03	1.84	0.16	14.09
CZC-2	14.38	0.03	0.76	11.35	7.94	3.10	13.93	0.32	0.09	9.78	0.01	0.02	0.01	30.49
CZC-3	0.24	0.01	0.09	2.60	1.78	61.52	0.35	0.02	0.02	0.03	0.01	0.02	0.01	27.17
CZC-4	32.22	0.17	2.13	12.18	7.44	2.32	6.36	0.21	0.51	6.36	0.01	0.08	0.05	21.82
CZC-5	19.02	0.13	2.00	12.01	7.13	2.58	5.30	0.89	1.52	19.20	0.01	0.04	0.03	20.09
CZC-6	38.72	0.49	5.99	7.27	2.66	15.63	4.72	0.16	0.86	4.36	0.03	1.18	0.12	15.45
CZC-7	33.62	0.11	1.30	8.69	7.38	2.23	12.40	0.04	0.09	0.08	0.01	0.28	0.04	29.03
CZC-8	28.41	0.23	1.70	7.08	5.42	22.49	5.03	0.06	0.14	0.88	0.01	0.27	0.06	23.44
CZC-9	15.14	0.06	1.50	14.88	13.32	1.44	8.15	0.05	0.03	1.27	0.01	0.38	0.03	35.99
CZC-10	23.26	0.01	0.18	13.61	12.69	7.59	1.57	0.09	0.01	3.86	0.01	0.01	0.01	29.64
CZC-11	62.98	0.86	12.87	7.98	0.03	0.05	0.10	0.33	2.05	2.88	0.28	4.71	0.23	0.15
CZC-12	1.81	0.01	0.11	14.05	1.45	8.08	23.94	0.80	0.02	0.12	0.01	0.04	0.01	41.21
CZC-13	35.51	0.22	2.90	21.68	1.84	0.03	0.16	1.20	2.80	19.59	0.11	0.02	0.07	10.90
CZC-14	5.20	0.09	1.85	8.60	1.24	15.24	23.18	0.36	0.81	0.59	0.01	0.04	0.04	35.10
CZC-15	2.58	0.04	0.48	32.64	0.23	3.77	7.60	0.27	0.19	0.08	0.01	0.01	0.03	44.32

Note: The content unit is % for major elements and dimensionless for others.

5 Results

5.1 Major elements, trace elements, and REEs

The major element composition of ores from the Chazangcuo deposit is shown in Table 1. The CuO, PbO, and ZnO contents in 15 ores varied significantly from 0.03% to 13.32% (average: 5.15%), from 0.03% to 61.52% (average: 9.78%), and from 0.10% to 23.94% (average: 7.56%), respectively. The SO₃, TFe₂O₃, and Al₂O₃ contents ranged from 0.15% to 44.32% (average: 25.26%), 2.60%–32.64% (average: 12.47%), and 0.09%–12.87% (average: 2.83%), respectively. The CuO, PbO, ZnO, SO₃, TFe₂O₃, Al₂O₃, MnO, and MgO contents were positively correlated with the copper-lead-zinc ore grades, suggesting chalcopyrite, pyrite, galena, and sphalerite mineralization. The SiO₂ content in the samples ranged from 0.24% to 62.98%, averaging 23.10%, while the CaO content varied from 0.03% to 19.59%, with an average of 5.19%. Both exhibited negative correlations with the copper, lead, and zinc grades.

The trace element and REE compositions of ores from the Chazangcuo deposit are detailed in Table 2. The ore samples displayed a relative scarcity of large-ion lithophile elements (LILEs) like Rb, Sr, and Ba and high-field-strength elements (HFSEs) such as Nb, Ta, Zr, and Hf (Figure 4A). The total REE content in

the samples varied from 9×10^{-6} to 119.45×10^{-6} , averaging 45.38×10^{-6} . The light rare earth element (LREE) content ranged from 7×10^{-6} to 104.9×10^{-6} , the heavy rare earth element (HREE) content from 2×10^{-6} to 14.55×10^{-6} , with the LREE-to-HREE ratio fluctuating between 2.53 and 8.72. This indicates a relative enrichment of LREEs and a deficit of HREEs (Figure 4B). The normalized (La/Yb)_N and (Gd/Yb)_N ratios averaged 7.41 and 1.52, respectively, highlighting a significant differentiation between LREEs and HREEs. The normalized (La/Sm)_N and (Sm/Nd)_N ratios averaged 4.03 and 0.73, respectively, denoting a high degree of REE fractionation. The ore samples exhibited an average δEu value of 1.16, suggesting slight positive Eu anomalies, and their δCe values ranged from 0.01 to 0.99, with an average of 0.76.

5.2 Fluid inclusions

Fluid inclusions within the Chazangcuo deposit exhibit notable similarities. Compared to those in porphyry and skarn deposits, they present significantly lower abundance, typically below 100/mm². They are small, mainly ranging from two to 7 μm individually, with a few extending to 10–20 μm . These fluid inclusions are largely irregular, elliptical, and elongated in shape, followed by negative crystal shapes and rounded forms. Some of them exhibit

TABLE 2 Analytical results of trace elements and REEs.

Sample no.	CZC-1	CZC-2	CZC-3	CZC-4	CZC-5	CZC-6	CZC-7	CZC-8	CZC-9	CZC-10	CZC-11
Ba	100	100	100	100	100	100	100	100	100	100	758
Rb	111	1.00	1.00	5.00	2.00	62.00	18.00	17.00	27.00	1.00	238
Nb	5.00	1.00	1.00	2.00	1.00	4.00	1.00	2.00	1.00	1.00	5.90
Ta	0.50	0.50	0.50	0.50	0.50	0.50	0.50	0.50	0.50	0.50	0.40
La	18.00	5.00	5.00	7.00	10.00	10.00	5.00	7.00	5.00	5.00	23.60
Ce	38.60	6.40	0.10	14.20	19.60	22.10	6.10	13.80	9.30	2.80	47.80
Sr	330	42.00	2.00	80.00	740	56.00	3.00	33.00	10.00	28.00	94.40
Nd	20.00	4.00	1.00	7.00	10.00	12.00	3.00	6.00	5.00	2.00	21.90
Sm	4.10	1.00	0.30	2.00	2.70	2.40	0.70	1.20	1.00	0.50	4.62
Zr	80.00	5.00	5.00	28.00	16.00	53.00	14.00	17.00	10.00	5.00	128
Hf	2.00	1.00	1.00	1.00	1.00	2.00	1.00	1.00	1.00	1.00	3.30
Tb	0.70	0.30	0.10	0.30	0.50	0.40	0.10	0.20	0.10	0.10	0.63
Y	21.00	12.00	1.00	11.00	16.00	10.00	2.00	5.00	3.00	5.00	21.00
Pr	4.90	0.90	0.30	1.90	2.30	2.80	0.80	1.70	1.20	0.50	5.78
Eu	1.70	0.40	0.30	0.40	1.00	0.50	0.30	0.30	0.30	0.30	1.20
Gd	4.20	1.30	0.50	1.90	2.80	2.20	0.50	1.20	0.80	0.60	4.45
Dy	4.10	2.00	0.50	2.20	3.10	2.00	0.50	1.00	0.70	0.90	3.87
Ho	0.80	0.40	0.10	0.40	0.70	0.40	0.10	0.20	0.10	0.20	0.80
Er	2.10	1.20	0.30	1.40	1.90	1.20	0.30	0.70	0.30	0.60	2.19
Tm	0.30	0.20	0.10	0.20	0.20	0.20	0.10	0.10	0.10	0.10	0.32
Yb	1.70	1.40	0.30	1.30	1.40	1.00	0.30	0.50	0.30	0.60	1.99
Lu	0.20	0.20	0.10	0.20	0.20	0.10	0.10	0.10	0.10	0.10	0.30
ΣREE	101.40	24.7	9.00	40.4	56.4	57.3	17.9	34.00	24.30	14.30	119.45
ΣLREE	87.30	17.7	7.00	32.5	45.6	49.8	15.9	30.00	21.80	11.10	104.90
ΣHREE	14.10	7.00	2.00	7.90	10.8	7.50	2.00	4.00	2.50	3.20	14.55
LREE:HREE	6.19	2.52	3.50	4.11	4.22	6.64	7.95	7.50	8.72	3.46	7.20
δEu	1.24	1.07	2.35	0.61	1.10	0.65	1.47	0.75	0.99	1.67	0.79
δCe	0.97	0.67	0.01	0.92	0.94	0.99	0.66	0.93	0.88	0.34	0.95
Eu*	18.62	5.07	1.73	8.79	12.32	10.40	2.76	5.39	4.10	2.44	20.43
Ce*	49.11	11.75	9.29	19.07	25.55	27.60	11.34	18.25	12.98	10.11	61.75
(La:Sm) _N	2.76	3.14	10.48	2.20	2.32	2.62	4.49	3.66	3.14	6.29	3.21

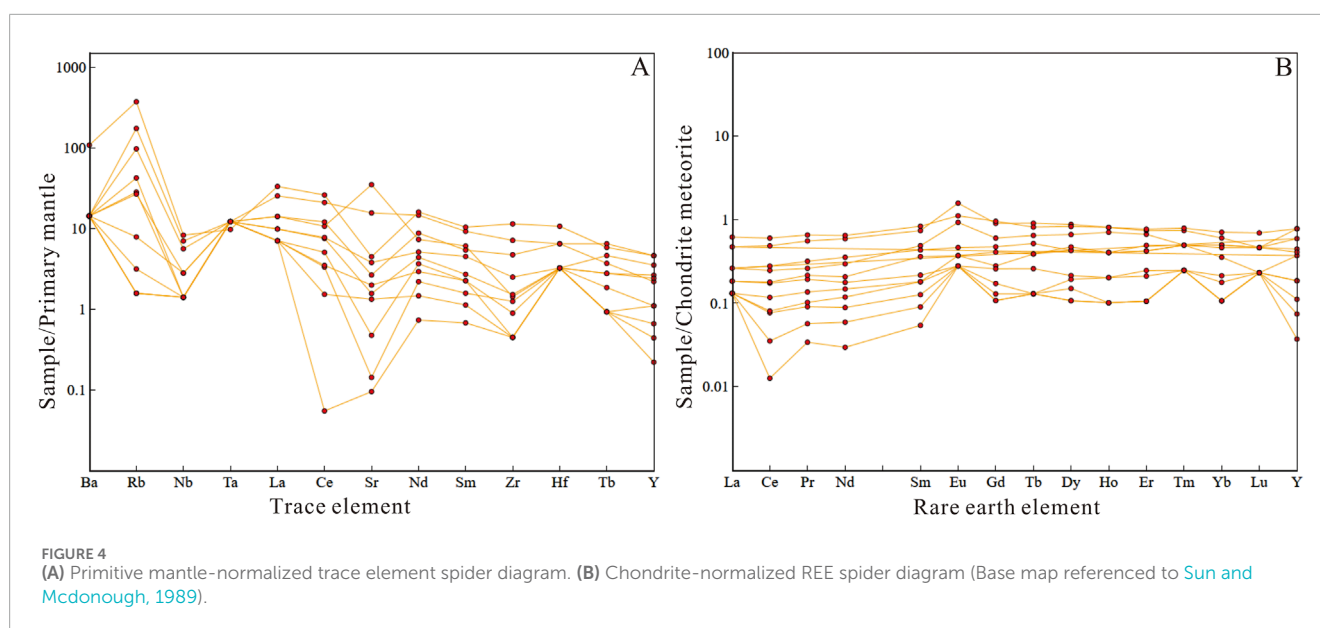
(Continued on the following page)

TABLE 2 (Continued) Analytical results of trace elements and REEs.

Sample no.	CZC-1	CZC-2	CZC-3	CZC-4	CZC-5	CZC-6	CZC-7	CZC-8	CZC-9	CZC-10	CZC-11
(La:Yb) _N	7.13	2.40	11.23	3.63	4.81	6.74	11.23	9.43	11.23	5.61	7.99
(Sm:Nd) _N	0.63	0.76	0.92	0.87	0.83	0.61	0.71	0.61	0.61	0.76	0.64
(Gd:Yb) _N	1.99	0.74	1.34	1.17	1.61	1.77	1.34	1.93	2.15	0.80	1.80

Note: The content unit is 10⁻⁶.

for trace elements and REEs, and dimensionless for others.



dark bubbles, hinting at a minor impurity content (Figure 5). The fluid inclusions are primarily of vapor-liquid types (approximately 99% and above), with a small presence of daughter mineral-bearing multiphase inclusions and mono-phase liquid inclusions. Among vapor-liquid inclusions, those rich in the liquid phase are predominant, with long axis measuring between 2 and 16 μm , largely concentrated at 5 to 8 μm . The vapor-liquid inclusions exhibit vapor-to-liquid ratios varying from about 20% to 80%, with an average ranging from around 30%–40%. Daughter mineral-bearing three-phase inclusions are less common (below 1%), mostly showcasing irregular shapes. The daughter minerals are typically square in shape, with a slight green tint.

The fluid inclusions from the ore-bearing quartz veins and ore-bearing calcite veins in the Chazangcuo deposit exhibit homogenization temperatures varying from 240°C to 280°C and from 220°C to 240°C, respectively, which correspond to the quartz-sulfide and calcite-sulfide mineralization stages of the deposit, respectively. The fluid inclusions in the ore-bearing quartz veins and the ore-bearing calcite veins have average salinity (w (NaCl, equivalent)) of 3.989% and 5.188%, respectively.

5.3 Sulfur and lead isotopes

The ore sulfides in the Chazangcuo deposit exhibit $\delta^{34}\text{S}$ values varying from 0.56‰ to 3.34‰, with an average of 2.60‰ and a range of 2.78‰, as derived from 13 samples. Specifically, four chalcopyrite samples yielded $\delta^{34}\text{S}$ values ranging between 0.56‰ and 3.07‰, with an average of 2.02‰ and a range of 2.51‰; three galena samples exhibited $\delta^{34}\text{S}$ values from 2.98‰ to 3.32‰, with an average of 3.12‰ and a range of 0.34‰, and one sphalerite sample displayed a $\delta^{34}\text{S}$ value of 3.34‰ (Table 3). The frequency histogram showing the sulfur isotope composition of ore sulfides presents a tower-like distribution, suggesting a relatively uniform sulfur isotope composition and stable metallogenic environments and metallogenic physicochemical conditions.

The lead isotope analysis results of metal sulfides (Table 3) indicate that the $^{206}\text{Pb}/^{204}\text{Pb}$, $^{207}\text{Pb}/^{204}\text{Pb}$, and $^{208}\text{Pb}/^{204}\text{Pb}$ ratios vary from 18.04 to 18.76 (average: 18.49; range: 0.72), 15.67–15.79 (average: 15.73; range: 0.12), 38.84–39.25 (average: 39.08; range: 0.41), respectively, exhibiting minor variations. The variation of Pb isotope μ and ω value of sulfide can provide information on the geological process of the geological body and reflect the source of Pb.

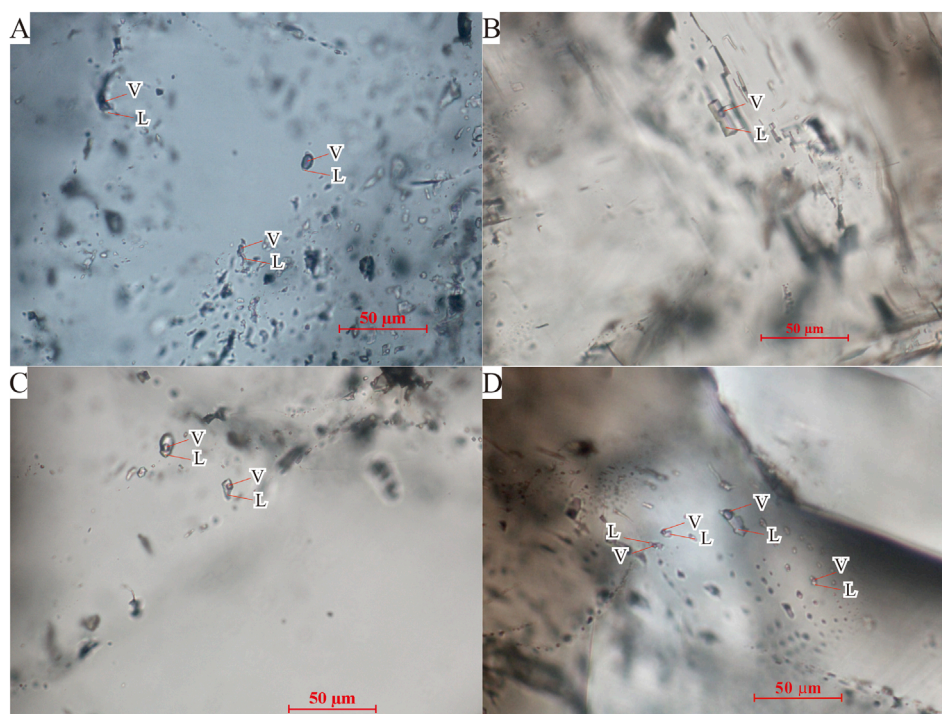


FIGURE 5
Microscope images of fluid inclusions from the Chazangcuo deposit. (A, B) Vapor-liquid inclusions from ore-bearing calcite. (C, D) Vapor-liquid inclusions from ore-bearing quartz veins.

According to Equations 1, 2 (Wu et al., 2002), the μ and ω values of lead isotopes in eight metal sulfide samples ranged from 9.61 to 9.82 (average: of 9.71) and 38.78 to 41.81 (average: 39.95), respectively. This generally reflects that the Pb source has the characteristics of the upper crustal source area.

$$\mu = \frac{[(^{206}\text{Pb}/^{204}\text{Pb})_t - a_0] / (e^{\lambda_{1T}} - e^{\lambda_{1t}})}{[(^{206}\text{Pb}/^{204}\text{Pb})_t - 9.307] / (e^{\lambda_{1T}} - e^{\lambda_{1t}})} \quad (1)$$

$$\omega = \frac{[(^{208}\text{Pb}/^{204}\text{Pb})_t - c_0] / (e^{\lambda_{3T}} - e^{\lambda_{3t}})}{[(^{208}\text{Pb}/^{204}\text{Pb})_t - 29.746] / (e^{\lambda_{3T}} - e^{\lambda_{3t}})} \quad (2)$$

Where: t is the time experienced after the mineral common lead is separated from the source region. $\lambda_1 = 0.155125 \times 10^{-9} \text{a}^{-1}$, $\lambda_2 = 0.98485 \times 10^{-9} \text{a}^{-1}$, $\lambda_3 = 0.049745 \times 10^{-9} \text{a}^{-1}$.

5.4 Electron probe microanalysis

5.4.1 Chalcopyrite

The $w(\text{Cu})$, $w(\text{Fe})$, and $w(\text{S})$ values of chalcopyrite ranged from 33.562% to 34.952% (average: 34.377%), 30.495%–31.154% (average: 30.841%), 32.112%–34.722% (average: 33.908%), respectively. The $w(\text{Zn})$ and $w(\text{Co})$ values ranged from 0.054% to 0.174% (average: 0.106%) and 0.045%–0.066% (average: 0.053%), respectively (Table 4). Compared to the theoretical values of Cu, Fe, and S in chalcopyrite ($w(\text{Cu}) = 34.56\%$, $w(\text{Fe}) = 30.52\%$, and $w(\text{S})$

$= 34.92\%$), chalcopyrite in this study shows relatively Fe-rich and slightly Cu- and S-deficient characteristics (Figures 6A–C).

Investigating the Zn incorporation in chalcopyrite involved analyzing the correlation between Zn, Fe, and Cu. The analytical results reveal a lack of significant correlation between Zn-Fe and Cu-Fe, while a slight negative correlation was observed between Zn and Cu. This pattern implies that Zn might have predominantly replaced Cu in chalcopyrite through isomorphism, leading to generally high Zn content. The reduced Zn content in some chalcopyrite samples could be attributed to their formation in different periods, as isomorphic substitution varies across different episodes of mineral formation (Zhang H. S. et al., 2018; Li et al., 2019).

5.4.2 Pyrite

The $w(\text{Fe})$ and $w(\text{S})$ values of pyrite ranged from 47.874% to 61.084% (average: 56.654%) and 38.102%–52.772% (average: 43.375%), respectively. Its $w(\text{Cu})$ and $w(\text{Zn})$ values varied from 0.006% to 0.074% (average: 0.041%) and 0.032%–0.045% (average: 0.038%), respectively. Its $w(\text{As})$ and $w(\text{Co})$ values ranged from 0.031% to 0.083% (average: 0.065%) and 0.116%–0.225% (average: 0.153%), respectively, and its $w(\text{Ni})$ values spanned 0.011%–0.192%, averaging 0.079% (Table 5). Compared to the theoretical values of Fe and S in pyrite ($w(\text{Fe}) = 46.55\%$, $w(\text{S}) = 53.45\%$), pyrite in this study shows Fe-rich and S-deficient characteristics. The S deficiency of pyrite is beneficial to the enrichment of metal elements (Figures 6D, E).

To elucidate the occurrence forms of various elements in pyrite, correlation analyses were conducted on the trace element

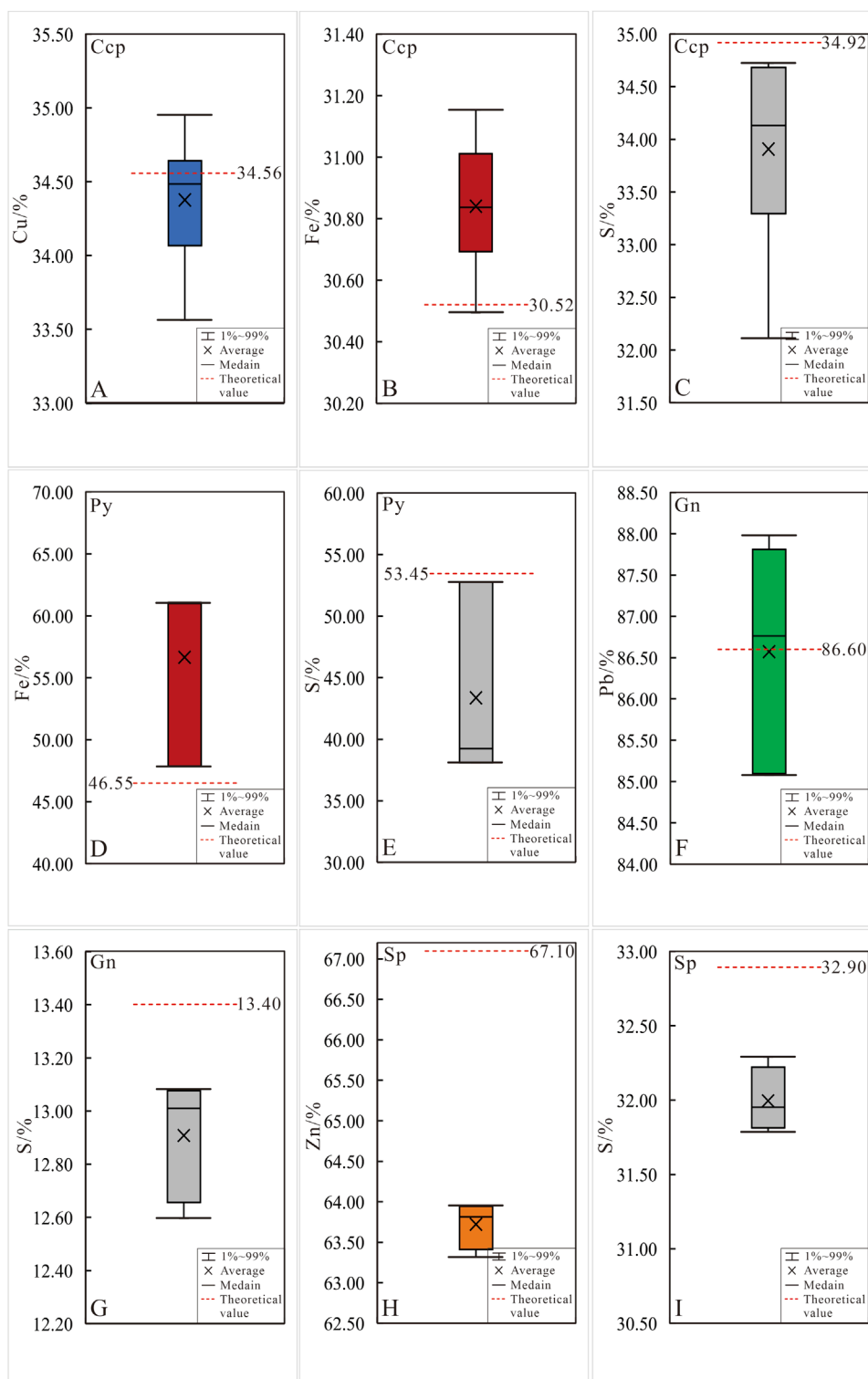


FIGURE 6

Box plots showing the element contents of chalcopyrite, pyrite, galena, and sphalerite. (A) Box plot of Cu content in chalcopyrite by electron probe microanalysis. (B) Box plot of Fe content in chalcopyrite by electron probe microanalysis. (C) Box plot of S content in chalcopyrite by electron probe microanalysis. (D) Box plot of Fe content in pyrite by electron probe microanalysis. (E) Box plot of S content in pyrite by electron probe microanalysis. (F) Box plot of Pb content in galena by electron probe microanalysis. (G) Box plot of S content in galena by electron probe microanalysis. (H) Box plot of Zn content in sphalerite by electron probe microanalysis. (I) Box plot of S content in sphalerite by electron probe microanalysis.

TABLE 3 Sulfur and lead isotope characteristics.

Sample no.	Mineral	$\delta^{34}\text{S}/\text{‰}$	$^{206}\text{Pb}/^{204}\text{Pb}$	$^{207}\text{Pb}/^{204}\text{Pb}$	$^{208}\text{Pb}/^{204}\text{Pb}$	T/Ma	μ	ω	Th/U	$\Delta\alpha$	$\Delta\beta$	$\Delta\gamma$
CZC-3	Galena	2.98	18.55	15.79	38.92	297	9.82	39.53	3.9	82.16	30.47	46.29
CZC-4	Chalcopyrite	3.07	18.46	15.72	39.15	278	9.69	40.33	4.03	76.91	25.9	52.47
CZC-5	Sphalerite	3.34	18.37	15.67	39.10	282	9.61	40.16	4.04	71.66	22.64	51.13
CZC-7	Galena	3.32	18.63	15.68	39.18	108	9.6	39.07	3.94	86.83	23.29	53.28
CZC-8	Chalcopyrite	2.31	18.04	15.74	38.84	592	9.79	41.81	4.13	52.41	27.21	44.14
CZC-9	Galena	3.05	18.76	15.78	39.05	138	9.78	38.78	3.84	94.41	29.82	49.78
CZC-10	Chalcopyrite	2.13	18.68	15.76	39.17	170	9.75	39.53	3.92	89.43	28.49	52.83
CZC-11	Chalcopyrite	0.56	18.45	15.68	39.25	237	9.62	40.40	4.06	81.29	23.58	57.98

content in pyrite. The analytical results show a significant negative correlation between Fe and S, certain correlations between Fe and both Co and Ni, and negligible correlations between Fe and Cu, Zn, and As. Table 5 indicates that Cu, Zn, and As in pyrite in the study area likely occur in multiple forms rather than merely simple isomorphs.

5.4.3 Galena

The $w(\text{Pb})$ and $w(\text{S})$ values of galena ranged from 85.077% to 87.979% (average: 86.573%) and 12.596%–13.081% (average: 12.908%), respectively, and its $w(\text{Cu})$ and $w(\text{Zn})$ values ranged from 0.008% to 0.138% (average: 0.073%) and 0.002%–0.029% (average: 0.020%), respectively (Table 6). Compared to the theoretical values of Pb and S in galena ($w(\text{Pb}) = 86.60\%$, $w(\text{S}) = 13.40\%$), galena in this study shows deficit S and slightly deficit Pb (Figures 6F, G).

5.4.4 Sphalerite

The $w(\text{Zn})$ and $w(\text{S})$ values of sphalerite ranged from 54.010% to 63.949% (average: 61.114%) and 31.788%–33.753% (average: 32.499%), respectively. Its $w(\text{Fe})$ and $w(\text{Cu})$ values ranged from 2.173% to 11.411% (average: 4.988%) and 0.030%–0.520% (average: 0.264%), respectively, and its $w(\text{Cd})$ and $w(\text{Mn})$ values ranged from 0.227% to 0.571% (average: 0.436%) and 0.073%–0.852% (average: 0.259%), respectively (Table 7). Compared to the theoretical values of Zn and S in sphalerite ($w(\text{Zn}) = 67.10\%$, $w(\text{S}) = 32.90\%$), sphalerite in this study shows deficit Zn and slightly deficit S (Figures 6H, I).

Element Cd typically occurs as an isomorph in sphalerite, with a stable content range. It exhibits similar geochemical behavior to Zn. Schwartz (2000) suggests that the Cd content in volcanogenic massive sulfide (VMS) deposits ranges from 100×10^{-6} to $10,000 \times 10^{-6}$, with an average of $2,360 \times 10^{-6}$. Given that the Cd content in the study area ranged from $4,010 \times 10^{-6}$ to $5,710 \times 10^{-6}$, averaging $5,199 \times 10^{-6}$, the Chazangcuo deposit is of a VMS type (Schwartz, 2000).

6 Discussion

6.1 Mineralization periods

In this study, the mineralization process of the Chazangcuo deposit is segmented into three distinct periods and four stages based on the crosscutting relationships of veins, mineral assemblages, and ore textures (Figure 7).

- (1) The magmatic-hydrothermal mineralization period, including the quartz-pyrite-sphalerite mineralization stage (I). This period witnessed the formation of quartz, pyrite, and sphalerite. The quartz formed in this stage occurs as xenomorphic irregular and elongated grains, consisting of microfine quartz, metallic minerals, sericite, and clay minerals in terms of internal composition. Subject to dynamic action, microcracks and fissures are prevalent within the quartz, and larger quartz grains are typically encased by granular quartz aggregates or carbonate minerals, chlorite, and metallic minerals as fillings. The pyrite formed in this stage, characterized by hypidiomorphic to xenomorphic granular

TABLE 4 Electron probe microanalysis results of chalcopyrite.

CuFeS ₂		Sb	Ag	Au	Mn	Co	Zn	S	Fe	Cu	As	Se
CZC-2	ave=5	-	0.012	0.014	-	0.055	0.054	33.687	31.154	34.470	0.037	0.064
CZC-5	ave=5	-	0.012	-	-	0.047	0.108	34.272	30.760	34.952	0.061	0.042
CZC-6	ave=5	-	0.018	0.021	-	0.045	0.099	32.112	30.777	33.562	0.143	0.019
CZC-7	ave=5	-	-	0.033	-	0.052	0.080	33.990	30.897	34.539	0.038	0.088
CZC-14	ave=5	-	0.139	0.020	-	0.066	0.174	34.668	30.963	34.501	0.016	0.062
CZC-15	ave=1	-	0.071	0.034	-	0.052	0.121	34.722	30.495	34.237	-	-

TABLE 5 Electron probe microanalysis results of pyrite.

FeS ₂		Co	Zn	Ni	Cu	S	Fe	As
CZC-5	ave=4	0.118	0.045	0.0305	0.043	52.772	47.874	0.083
CZC-14	ave=5	0.225	0.032	0.112	0.074	39.252	61.005	0.081
CZC-15	ave=5	0.116	0.036	0.033	-	38.102	61.084	0.031

textures, is frequently found on the surfaces of chalcopyrite grains. The pyrite is enveloped by chalcopyrite, with sphalerite association and metasomatism observed at grain edges and within fissures (Figure 8A).

- (2) The hydrothermal mineralization period, including the medium-low-temperature hydrothermal sulfide mineralization stage (II) and the chlorite-carbonate mineral mineralization stage (III). The sulfides formed in stage II primarily consist of pyrite, chalcopyrite, sphalerite, and galena and are frequently associated with quartz. These sulfides, predominantly sparsely disseminated, are disorderly distributed within rock fissures. The chalcopyrite, encapsulated by pyrite and sphalerite on their grain surfaces, is haphazardly distributed in gangue minerals. The galena in the sulfides displays association and metasomatism with sphalerite, chalcopyrite, and pyrrhotite grains. This stage represents the dominant mineralization stage (Figure 8B). The chlorite-carbonate mineral mineralization stage (III) saw the filling and metasomatism of aggregates, consisting of chlorite and carbonate minerals, along rock fissures (Figure 8C).
- (3) The supergene period, including the supergene oxidation stage (IV). This period witnessed the emergence of secondary oxidized minerals represented by malachite and limonite (Figure 8D).

6.2 Source of metallogenic materials

The trace element and REE ratios are insightful indicators of material sources in a magma source. The study area exhibits an average Nb/Ta ratio of 4.80, lower than the typical crustal value of

11.3, much lower than the mantle source characteristics (17 ± 1) (Green, 1995; Rudnick and Fountain, 1995), an average Zr/Hf ratio of 18.66, which is lower than the continental crust value of 33 and far lower than the mantle-derived rock ratio (36.3) (Hofmann, 1988; Taylor and McLennan, 1995), and an average Rb/Sr ratio of 1.25, which is consistent with the characteristics of crust source (Rb/Sr < 0.5) (Taylor and McLennan, 1995). These ratios suggest that the materials in the study area are essentially derived from the crust and experienced extensive crystallization differentiation.

Investigating the sulfur isotopic composition of metal sulfides within a deposit aids in identifying the source of ore-forming materials and exploring the formation process of the deposit (Sakai, 1968; Ohmoto, 1986). Based on Ohmoto's theoretical models, the $\delta^{34}\text{S}$ values of sulfides can roughly reflect the total sulfur isotopic composition ($\Sigma\delta^{34}\text{S}$) of hydrothermal fluids in a system with low oxygen fugacity in the case of a lack of sulfates and mineral assemblages composed of pyrite, sphalerite, galena, and chalcopyrite. In the Chazangcuo deposit, no sulfate mineral has been identified through field geological surveys and microscopic examinations of thin sections. In contrast, this deposit hosts large quantities of sulfide mineral assemblages consisting of pyrite, sphalerite, galena, and chalcopyrite. Furthermore, the pyrite and galena share relatively similar $\delta^{34}\text{S}$ values, indicating nearly equilibrium sulfur isotopic conditions. Therefore, the sulfur isotopic composition of metal sulfides in the Chazangcuo deposit fairly represents the overall sulfur isotopic composition of the metallogenic hydrothermal fluid system of the deposit. The $\delta^{34}\text{S}$ values decrease in an order of pyrite, sphalerite, chalcopyrite, and galena, suggesting that sulfur isotope fractionation among sulfides has achieved thermodynamic equilibrium (Zheng et al., 2000).

Studies have indicated sulfur in hydrothermal deposits primarily originates from three sources: mantle or deep crust, bacterial reduction in an open sedimentary environment, and evaporates from ocean water and seawater (Ohmoto, 1972; Seal, 2006). Sulfur derived from the first source exhibits $\delta^{34}\text{S}$ values of approximately $0\% \pm 3\%$, which fluctuate narrowly and typically show a tower-like distribution. Sulfur from the second source generally has significantly negative $\delta^{34}\text{S}$ values, which vary greatly. In contrast, sulfur in evaporate usually has $\delta^{34}\text{S}$ values of around 20‰. For the copper-lead-zinc ore sulfides in the Chazangcuo deposit, $\delta^{34}\text{S}$ values varying between 0.56‰ and 4.01‰ were obtained in this study, with an average of 2.75‰ and a range of 2.78‰.

TABLE 6 Electron probe microanalysis results of galena.

PbS		Ag	Sb	Co	Ni	Cu	Zn	S	Pb
CZC-2	ave=5	0	-	-	-	-	0.010	12.677	85.077
CZC-5	ave=5	0	-	-	0.061	0.101	0.028	13.075	87.979
CZC-6	ave=5	0	-	-	0.025	0.084	-	13.075	87.755
CZC-7	ave=5	0	-	-	0.030	0.015	0.029	12.596	85.100
CZC-14	ave=5	0	0.013	-	0.012	0.091	0.026	12.945	86.989
CZC-15	ave=5	0.041	-	-	0.021	0.138	0.028	13.081	86.538

TABLE 7 Electron probe microanalysis results of sphalerite.

ZnS		Sb	Cd	Mn	Co	Ni	S	Pb	As	Zn	Cu	Fe
CZC-2	ave=5	-	0.554	0.081	0.023	-	31.887	0.015	0.071	63.317	0.451	3.049
CZC-5	ave=5	-	0.554	0.073	0.029	-	32.290	0.013	0.034	63.697	0.520	2.173
CZC-6	ave=6	-	0.571	0.082	0.034	-	32.019	0.041	0.066	63.927	0.359	2.612
CZC-7	ave=5	-	0.401	0.116	0.028	-	31.788	-	-	63.949	0.030	2.411

This indicates a simple magmatic source of sulfur. Hydrothermal fluids from uncontaminated acid igneous magma, resulting from partial melting of crustal or upper mantle materials, exhibit $\delta^{34}\text{S}$ values varying from -3.00‰ to 7.00‰ (Ohmoto, 1986; Sun et al., 2020), aligning with those of metallogenic hydrothermal fluids in the Chazangcuo deposit ($0.56\text{‰} \sim 4.01\text{‰}$). Therefore, it can be inferred that the Chazangcuo deposit's sulfur likely originates from concealed intrusions or magmatic-hydrothermal fluids from the partial melting of the crust or upper mantle. The $\delta^{34}\text{S}$ values derived from this study are approximately distributed in a tower pattern (Figure 9). Compared to polymetallic deposits in the western section of Tibet's Gangdese (e.g., Zhuno ($-1.8\text{‰} \sim 1.5\text{‰}$), Ri'a ($2.1\text{‰} \sim 5.7\text{‰}$), Chagele ($-5.6\text{‰} \sim 2.6\text{‰}$), Narusongduo ($2.1\text{‰} \sim 5.9\text{‰}$), Xingaguo ($-5.0\text{‰} \sim 2.1\text{‰}$), Yaguila ($-3.2\text{‰} \sim 4.8\text{‰}$), Dongzhongla ($2.2\text{‰} \sim 5.7\text{‰}$)), the Chazangcuo deposit exhibit similar $\delta^{34}\text{S}$ values with a narrow variation range (Yang et al., 2010; Yu, 2011; Liu et al., 2011; Dai, 2017; Zhang Y. C. et al., 2018; Figure 10). Furthermore, the absence of sulfate-bearing minerals in strata in the Chazangcuo deposit excludes the sedimentary source of sulfur, also suggesting a magmatic origin of sulfur in ores.

Lead isotopic composition proves to be a crucial indicator of mineralization. Especially in sulfide deposits, lead isotopes convey extensive insights into mineralization, significantly influencing the determination of the deposits' ore-forming material sources, geochronology, relationship with magmatic activity, and genesis. Consequently, lead isotopic composition, as an effective tracer of ore-forming materials, has been extensively employed in research on sulfide deposits (Zartman and Doe, 1981; Zhang et al., 2006; Li et al., 2012). The variation in μ values provides insights into geological processes and the lead sources. Lead with high μ values ($\mu > 9.58$) or

radiogenic lead, as indicated by its position to the right of the zero isochron, typically stems from U- and Th-enriched upper crustal materials. Conversely, low μ and ω values suggest an upper mantle origin of lead, while low μ and high ω values are characteristic of a lower crustal source (Zhu et al., 1998; Wu et al., 2002). The high ω and μ values of ores in the study area imply a crustal origin of ore-forming materials. The Th/U ratios range from 3.84 to 4.13 (average: 3.98), indicating a stable lead isotopic composition and a simple ore-forming material composition.

The lead isotopic ratios of the Chazangcuo deposit are very close to those of the Zhazhalong, Narusongduo, and Dexin deposits in northern Gangdese, showing the characteristics of an upper crust source. The average $^{206}\text{Pb}/^{204}\text{Pb}$, $^{207}\text{Pb}/^{204}\text{Pb}$, and $^{208}\text{Pb}/^{204}\text{Pb}$ ratios of polymetallic sulfides in the Dexin deposit are 18.597, 15.686, and 39.061, respectively; those of polymetallic sulfides in the Zhazhalong deposit are 18.622, 15.714, and 39.169, respectively; and those of polymetallic sulfides in the Narusongduo deposit are 18.685, 15.734, and 39.273, respectively (Ke et al., 2019).

As shown in the $^{206}\text{Pb}/^{204}\text{Pb}$ - $^{207}\text{Pb}/^{204}\text{Pb}$ diagram (Figure 11A), all sample points from the Chazangcuo deposit aligned closely with the upper crustal evolution line, displaying a linear distribution with a gentle slope rather than dense overlapping and clustering. Moreover, the data points gradually diverged from the evolution line, differing significantly from the Pb distribution characteristics that are frequently found in multi-source regions. This pattern suggests that the ore-forming metals in the Chazangcuo deposit predominantly originate from the upper crust. The $^{206}\text{Pb}/^{204}\text{Pb}$ - $^{208}\text{Pb}/^{204}\text{Pb}$ isotopic diagram (Figure 11B) shows that the sample points exhibited a trend toward the orogenic belt and an upper crustal source from the upper mantle,

Metallogenic epoch	Magma-hydrothermal mineralization period	Hydrothermal mineralization period		Supergene
Metallogenic stage	Quartz-pyrite-sphalerite stage	Medium-low temperature polymetallic sulfide stage	Chlorite-carbonate mineral stage	Supergene oxidation stage
Quartz	Abundant	Abundant		
Pyrite	Abundant	Abundant		
Sphalerite	Abundant	Abundant		
Magnetite		Little		
Chalcopyrite	Medium	Abundant		
Bornite		Little		
Galena		Abundant	Abundant	
Chlorite			Little	
Calcite		Medium	Abundant	
Sericite			Trace	
Malachite				Trace
Limonite				Abundant





Annotation:  Abundant  Medium  Little  Trace

FIGURE 7
Mineralization periods and stages of the Chazangcuo deposit.

reinforcing the notion that upper crustal materials are the primary contributors of lead.

Zhu et al. (1998) demonstrated that the $^{207}\text{Pb}/^{204}\text{Pb}$ and $^{208}\text{Pb}/^{204}\text{Pb}$ ratios are particularly effective in reflecting variations in sources, whereas the $^{206}\text{Pb}/^{204}\text{Pb}$ ratio primarily responds to geochronological factors (Zhu et al., 1998). To underscore the changes in Th and Pb, as well as the interplays between the isotopic compositions of Th and Pb and those of U and Pb, this study deduced the tectonic setting and sources of the samples based on their positions on the $\Delta\beta$ - $\Delta\gamma$ diagram. As illustrated in the $\Delta\beta$ - $\Delta\gamma$ diagram of Pb isotopes (Figure 11C), the Pb isotopic signature of the metal sulfides in the Chazangcuo deposit is characteristic of the upper crust.

6.3 Metallogenic physicochemical conditions

Fluid density and volume are critical parameters for the analysis and calculation of fluid inclusions. The correlations of fluid density or volume with temperature and pressure can be outlined using the p-V-T relationship. As isovolumetric systems, fluid inclusions are composed of fluids with a certain density captured under certain temperature and pressure conditions (Liu and Duan, 1987; Liu, 2001; Pivetta et al., 2024). The inclusions of quartz veins in the Chazangcuo deposit exhibit significantly varying temperatures, spanning 218.6°C–352°C and averaging 268.7°C. As shown in Figure 12A, the temperature data are clustered within a range, displaying a distinct single-peak distribution. This indicates that hydrothermal mineralization of the quartz veins underwent a

medium-low-temperature stage. The salinity (w (NaCl, equivalent)) of the quartz veins ranges from 1% to 7.17%. Fluid density, derived from homogenization temperatures and salinity, measures between 0.787 and 0.863 g/cm³, leading to estimated metallogenic pressures ranging from 51.3×10^5 to 54.4×10^5 Pa. The calcite veins exhibit temperatures ranging from 140.8°C to 285.7°C, with an average of 233.4°C. As shown in Figure 12B, the temperature data spread across multiple ranges, exhibiting a multi-peak distribution, suggesting medium-low- and medium-temperature hydrothermal mineralization stages of the calcite veins. The salinity (w (NaCl, equivalent)), fluid density, and metallogenic pressure of the calcite veins range from = 1.5% to 9.34%, 0.845–0.912 g/cm³, and 26.1×10^5 – 27.7×10^5 Pa, respectively.

Overall, the ore-forming fluids of the Chazangcuo deposit transitioned from high to low homogenization temperatures and pressures from the early quartz-sulfide stage to the calcite-sulfide stage, while the fluid density trended upward. The salinity of fluid inclusions decreases with a decrease in the homogenization temperature, suggesting that the precipitation of ore-forming materials is primarily related to the blending of low-temperature, low-salinity fluids with the original ore-forming fluids (Ni et al., 2021; Li et al., 2022; Ren et al., 2023). Utilizing the measured temperatures and salinity data, a homogenization temperature vs. salinity diagram for the ore-forming fluids of the Chazangcuo deposit was plotted (Figure 13), revealing relatively consistent fluid inclusion temperatures and salinities (150–280°C and 3–8%, respectively). Considering data from the Dexin, Narusongduo, and Zhulang deposits, the fluid densities of these deposits predominantly fall within a range of 0.5–1 g/cm³, showcasing remarkable similarity

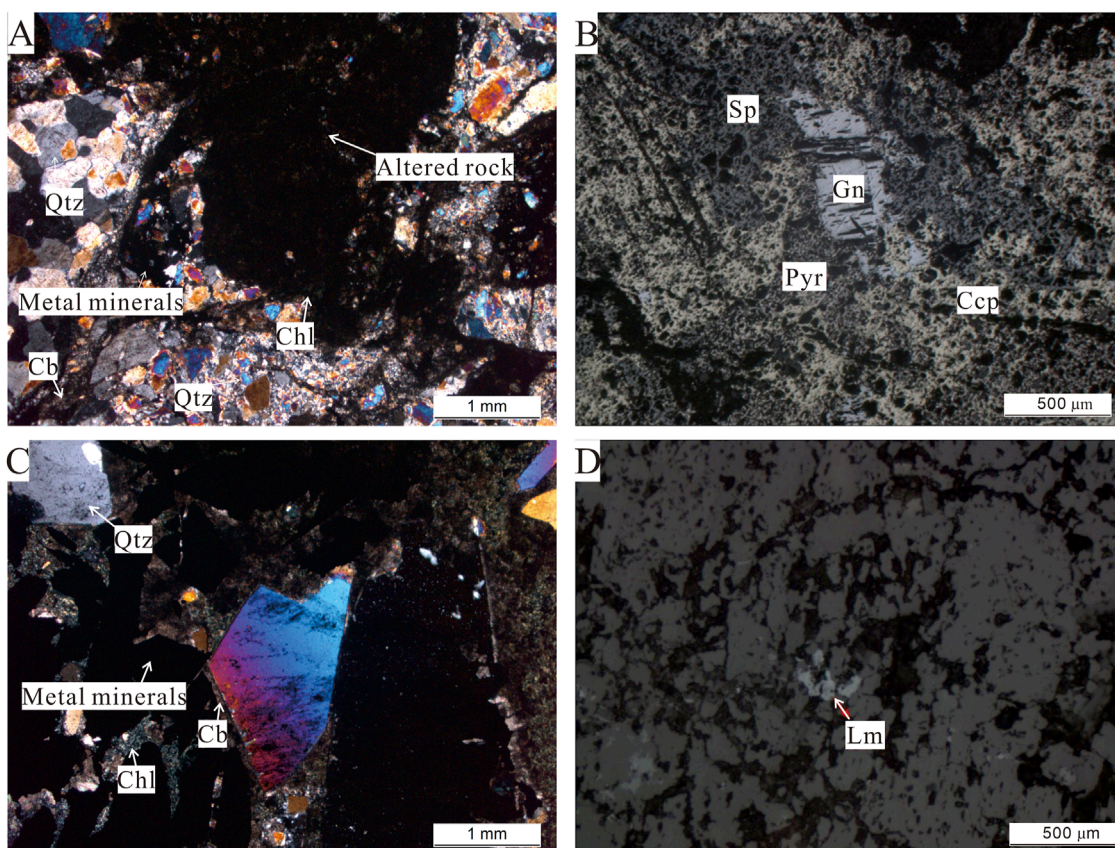


FIGURE 8 Characteristics of rocks and ores in different mineralization periods and stages of the Chazangcuo deposit. (A) Strong altered rock of Cu-Pb-Zn mineralization and cataclastic rock. (B) Pyrrhotite, sphalerite and Galena mixed on the surface of chalcopyrite aggregate. (C) Mineralized, cataclastic, chlorite and carbonated quartz veins. (D) Limonite is distributed in gangue minerals.

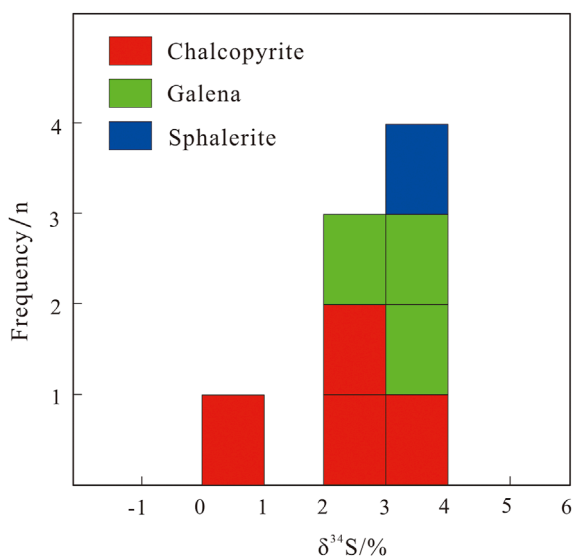


FIGURE 9 Frequency histogram showing the $\delta^{34}\text{S}$ values of the Chazangcuo deposit.

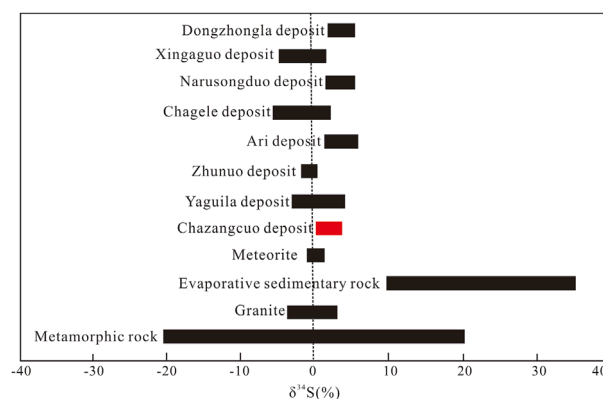
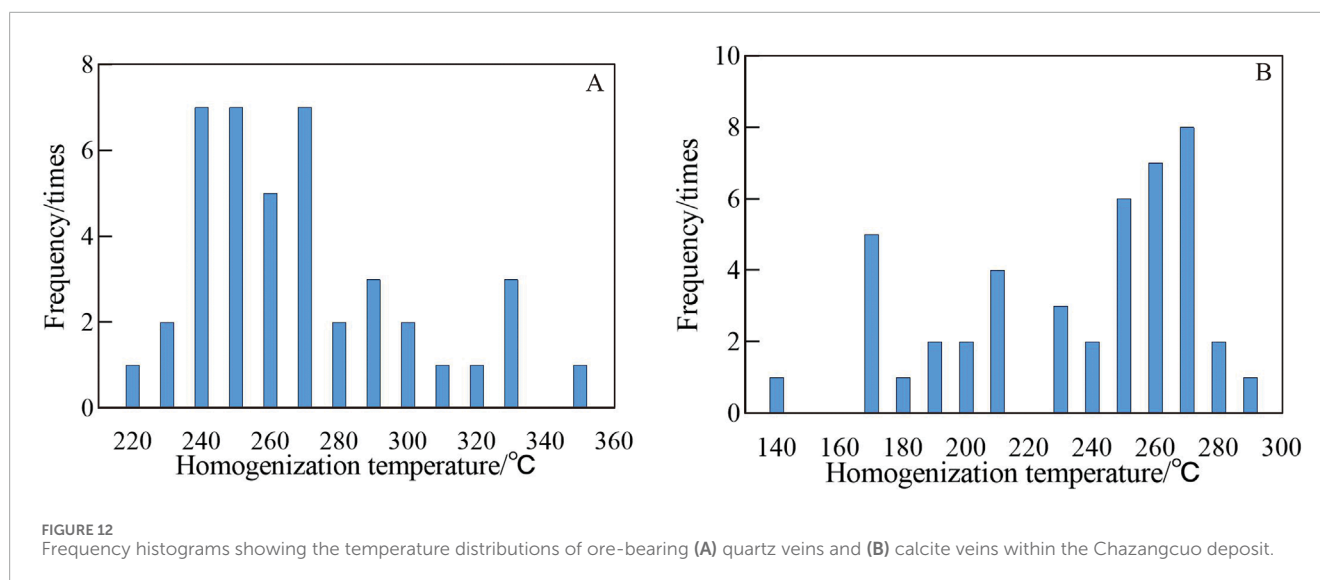
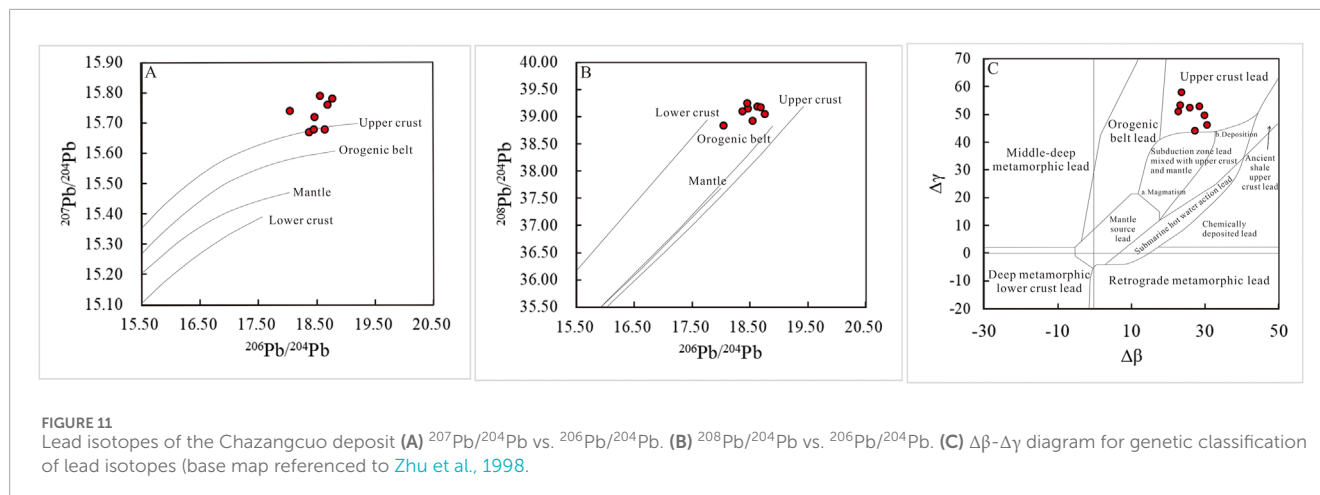


FIGURE 10 Distributions of $\delta^{34}\text{S}$ values of ore sulfides from the Chazangcuo deposit and its surrounding deposits.

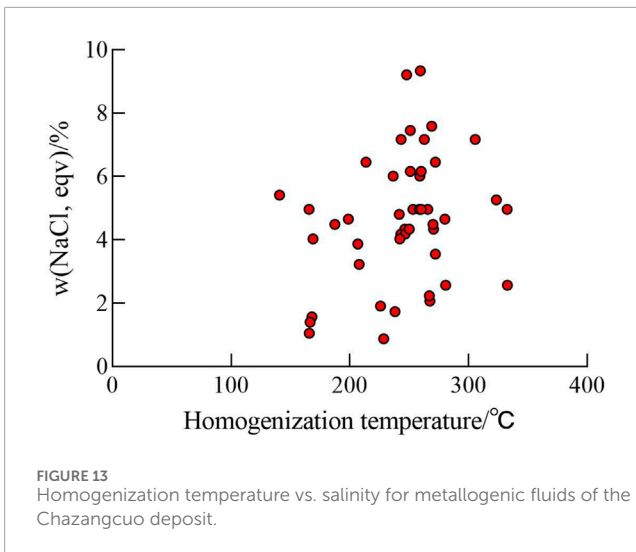
across various deposits, with the ore-forming fluids generally characterized by medium-low temperatures and low densities (Gong et al., 2019; Ke et al., 2019).



The elemental composition and ratios in pyrite can shed light on the type and formational conditions of a deposit, while the amalgamation of pyrite trace elements and Co content reflect the formation environment of a deposit ([Zheng et al., 2012](#); [Kong et al., 2015](#); [Li et al., 2019](#); [Shen et al., 2021](#)). Typically, high-temperature pyrite is enriched in siderophile and lithophile elements such as Cr, Ti, Co, Ni, Mo, Bi, Cu, and Zn; medium-temperature environments yield pyrite with higher-content chalcophile elements like Au, Ag, Cu, Pb, and Zn, while low-temperature pyrite is distinguished by the enrichment in high-activity chalcophile elements such as Hg, Sb, As, and Ag. Pyrite from the Chazangcuo deposit is characterized by elevated Hg, Sb, As, and Ag contents, suggesting that the deposit was formed in a low-temperature setting. The $w(\text{Fe})/w(\text{S}+\text{As})$ ratio of pyrite offers insights into its formation depth, with shallowly, moderately, and deeply formed pyrite typically showing $w(\text{Fe})/w(\text{S}+\text{As})$ ratios of 0.926, 0.863, and 0.846, respectively ([Wu et al., 2019](#); [Ge et al., 2023](#)). The $w(\text{Fe})/w(\text{S}+\text{As})$ ratios of pyrite in the study area range from 0.91 to 1.60, indicating a predominantly shallow formation environment of pyrite within the Chazangcuo deposit. Generally, hydrothermal pyrite exhibits sulfur

deficiency, whereas sedimentary pyrite is sulfur-rich or features an approximately theoretical value ($\text{S}/\text{Fe} = 1.999$). The S/Fe ratios of pyrite within the Chazangcuo deposit span 0.62 to 1.10, with an average of 0.79, suggesting a hydrothermal origin ([Lin et al., 2011](#)). The Co and Ni contents in pyrite also carry typomorphic significance. Specifically, sedimentary pyrite typically has low Co and Ni contents, with Co/Ni ratios <1 (average: 0.63), whereas hydrothermal pyrite has higher Co and Ni contents, with Co/Ni ratios ranging widely from 1.17 to 5. Volcanic exhalative massive sulfide deposits exhibit Co/Ni ratios between 5 and 50, averaging 8.7 ([Cook et al., 2009](#)). Within the Chazangcuo deposit, the Co/Ni ratios vary from 2.01 to 3.87, with an average of 3.16, consistent with hydrothermal origins. The Co-Ni mapping predominantly positions the sample points within the magma zone ([Figure 14A](#)), and the As-Co-Ni triangular diagram ([Figure 14B](#)) shows that most pyrite points fall within the magmatic-hydrothermal zone. Considering the geology of the study area, it can be inferred that pyrite in the study area is largely magmatic-hydrothermal in origin.

[Xiao et al. \(2008\)](#) posited that the distribution coefficient of trace element Co between associated chalcopyrite and pyrite within



a hydrothermal deposit correlates with temperature. Based on empirical equations for the chalcopyrite-pyrite geothermometer derived based on experiments (Equations 3 and 4), the K_D^{Ccp-Py} values in the study area were derived, ranging from 0.45 to 0.60. Accordingly, the formation temperatures of chalcopyrite and pyrite were determined at 227.8°C–271.8°C, indicating a medium-temperature metallogenic environment of the Chazangcuo deposit.

$$t = \frac{10^3}{1.2921 \times \lg K_D^{Ccp-Py} + 2.283} - 273.15 \quad (3)$$

$$K_D^{Ccp-Py} = \frac{w(Co)_{Ccp}}{w(Co)_{Py}} \times 1.53 \quad (4)$$

where t represents the formation temperature (°C) of chalcopyrite and pyrite; K_D^{Ccp-Py} denotes the distribution coefficient of trace element Co between chalcopyrite and pyrite, and $w(Co)_{Ccp}$ and $w(Co)_{Py}$ stand for the Co content in chalcopyrite and pyrite, respectively.

Additionally, the Zn/Fe ratio of sphalerite can be usually used as a geothermometer to reflect the formation temperature of a deposit (Li et al., 2017). The Zn/Fe ratios of below 10, between 10 and 100, and above 100 indicate moderately high-temperature (250–300°C), medium-temperature (150–250°C), and low-temperature (<150°C) environments, respectively. The Zn/Fe ratios of sphalerite in the Chazangcuo deposit range from 20.77 to 29.32, with an average of 25.27, generally indicating medium-low-temperature characteristics. Besides, the Zn/Cd ratio of sphalerite can be used as another geothermometer. The Zn/Cd ratios above 500, between 100 and 500, and below 100 imply high-temperature, medium-low-temperature characteristics, and low-temperature characteristics, respectively (Tian and Yang, 2022). The Zn/Cd ratios of sphalerite within the Chazangcuo deposit range from 111.99 to 159.55, with an average of 125.20, indicating medium-low-temperature characteristics. This coincides with the temperatures of fluid inclusions tested by Jiang et al. The Zn/Cd ratios of sphalerite range from 417 to 531 for volcanic sedimentary deposits, 252–330 for sedimentary and metamorphic deposits, 290–417 for VMS deposits, and 104–214 for volcanic hydrothermal and magmatic-hydrothermal deposits (Chen et al., 2024). The

Zn/Cd ratios of sphalerite within the Chazangcuo deposit range from 111.99 to 159.55, falling within the hydrothermal deposit range, more closely aligning with the characteristics of a magmatic-hydrothermal deposit.

Table 2 illustrates that the Eu, Sm, and Gd contents in the ore samples ranged from 0.3×10^{-6} to 1.7×10^{-6} (average: 0.61×10^{-6}), 0.3×10^{-6} to 4.62×10^{-6} (average: 1.87×10^{-6}), and 0.50×10^{-6} to 4.45×10^{-6} (average: 1.86×10^{-6}), respectively, all of which are low. The statistical results show that the Eu content is positively correlated with the Sm and Gd content. Therefore, the change in Eu in sphalerite is synchronous with Sm and Nd, suggesting that Eu in the ore-forming fluids occurred as Eu^{2+} in the sphalerite formation stage of the Chazangcuo deposit. The high Eu^{2+} content in the hydrothermal system suggests a medium-low temperature and strong reducing environment of the ore-forming fluids.

6.4 Ore genesis

Sulfide quartz veins represent the primary manifestation of ore bodies in the Chazangcuo deposit. Their occurrence is strictly governed by EW-NW-trending faults, which clearly distinguishes them from surrounding rocks. The mineral assemblages (quartz-pyrite-sphalerite-galena, chalcopyrite-pyrite-galena, chalcopyrite-galena-sphalerite, quartz-pyrite-sphalerite), ore textures (idiomorphic to xenomorphic granular texture, fracture filling texture, and metasomatic dissolution texture), and ore structures (massive, banded, disseminated, and stockwork structures) formed during the principal mineralization stage (the quartz-polymetallic sulfide stage) bear resemblance to those found in hydrothermal deposits.

The Chazangcuo deposit exhibits extensive alterations in surrounding rocks, such as silicification, pyritization, zoisitization, sericitization, siallitization, and chloritization. These alterations, formed in early to late stages and under high to low temperatures, are all observed, suggesting that magmatic-hydrothermal fluids were consistently involved throughout the metallogenic processes, thereby indicating that the ore body formation is attributable to magmatic-hydrothermal activity.

Investigations into major elements, trace elements, and REEs, alongside sulfur and lead isotopes, reveal low contents of trace elements and REEs within the Chazangcuo deposit. The Nb/Ta, Zr/Hf, and Rb/Sr ratios imply a predominantly crustal origin of materials. The $\delta^{34}\text{S}$ values exhibit a roughly tower-shaped distribution, primarily suggesting a uniform magmatic source of sulfur. The lead isotopic ratios and associated metrics suggest an upper crustal origin for the lead, generally indicating a crustal source for the ore-forming materials.

Investigation into fluid inclusions and electron probe analyses reveal that the metallic minerals in the Chazangcuo deposit are of magmatic-hydrothermal origin and their formation is closely linked to magmatic processes. Furthermore, the formation temperatures of sulfides in the deposit range from 150°C to 270°C. These suggest a medium-low mineralization temperature, shallow mineralization depth, a strongly reducing metallogenic setting, and medium-low-temperature and low-density ore-forming fluids.

Overall, ore bodies in the Chazangcuo deposit primarily occur as sulfide quartz veins, and the formation of the deposit

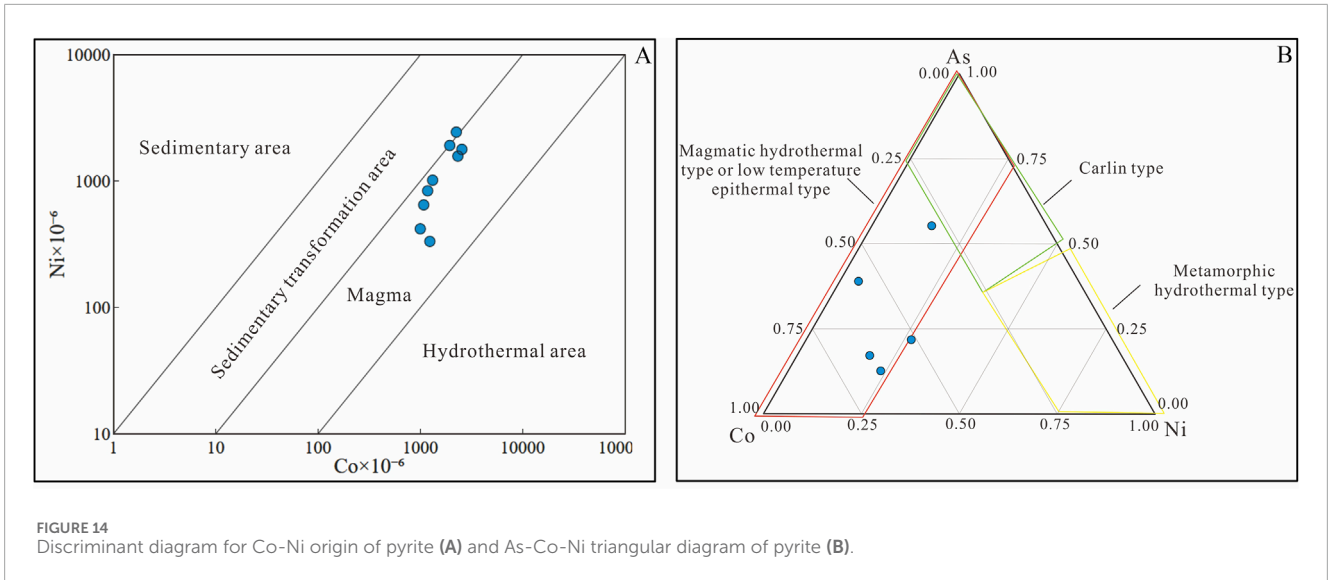


FIGURE 14 Discriminant diagram for Co-Ni origin of pyrite (A) and As-Co-Ni triangular diagram of pyrite (B).

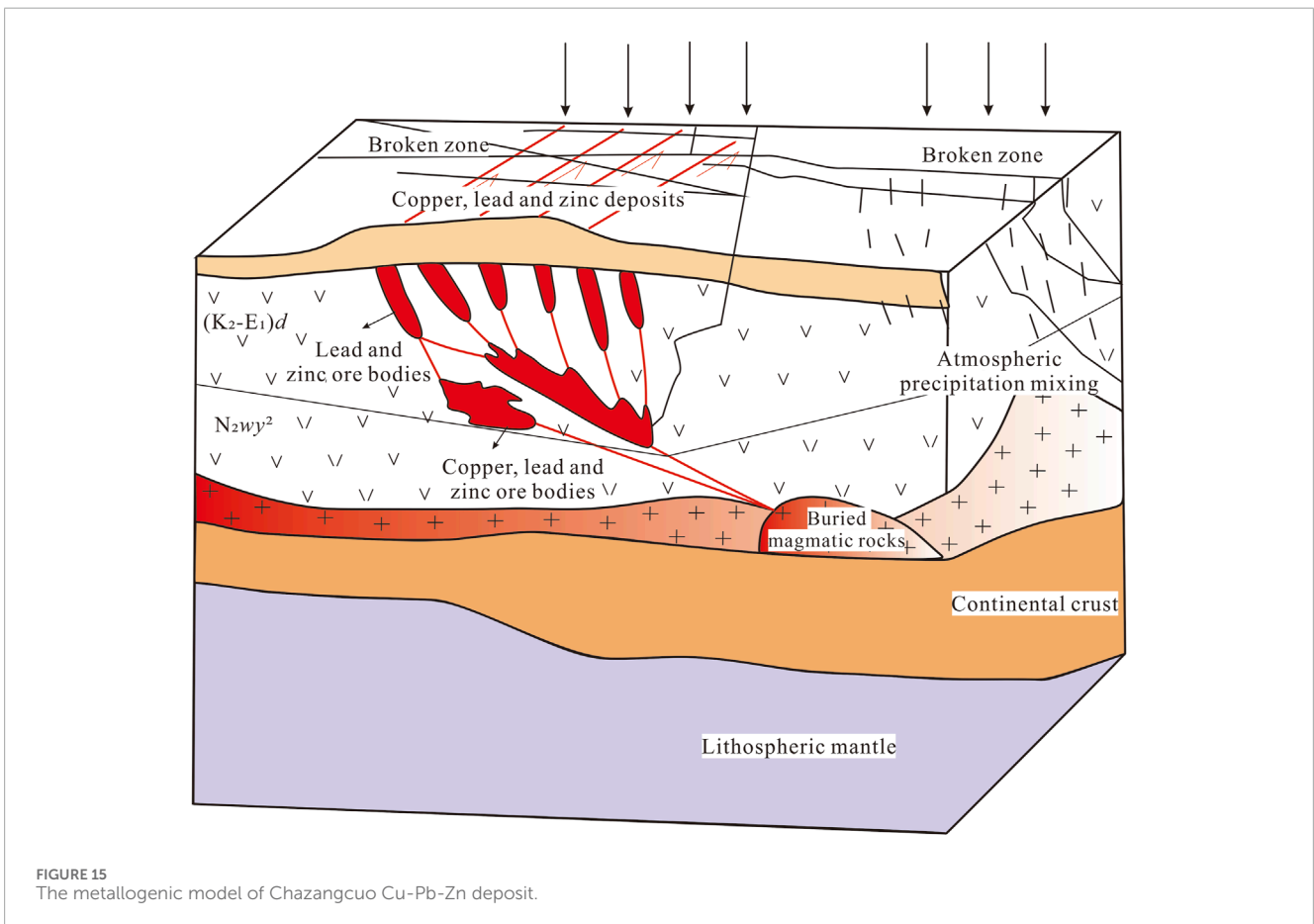


FIGURE 15 The metallogenic model of Chazangcuo Cu-Pb-Zn deposit.

is intimately associated with magmatic-hydrothermal activity. The deposit features medium-low-temperature and low-density ore-forming fluids and predominant upper crust-derived ore-forming materials. Furthermore, the mineralization occurred

at medium-low temperatures and shallow depths in a strongly reducing environment. All these classify the Chazangcuo deposit as an epithermal medium-low-temperature magmatic-hydrothermal type.

6.5 Mineralization model

The Neo-Tethys oceanic crust formed by the collision and subduction of the Indian continent and the Asian continent at about 65 Ma (Mo et al., 2005; Hou et al., 2006b), and the Indian continental crust subducted under the Lhasa block, resulting in a large-angle rotation of the oceanic plate (Chung et al., 2005) and asthenosphere upwelling (Wen et al., 2008). With the huge heat, the partial melting of the lower crust is induced, and the mantle-derived magma is mixed in with the crust-derived magma. They provide the initial magma source for the formation of acidic volcanic rocks and associated sub-volcanic rocks of the Linzizong Formation in the western part of the Gangdese (Jiang, 2018).

In the late stage of volcanism, the magma from the parent magma chamber emplaced and crystallized along the favorable structural parts such as volcanic edifices, and the crystallization process differentiated a large number of metal elements (Cu, Pb, Zn, Ag, Au, Mo, etc.) to form ore-bearing fluids. It carries a lot of heat in the process of ascending migration, which makes atmospheric precipitation form circulating convective groundwater. It extracts the metal elements in the surrounding rock of the volcanic rock, thus forming the ore-bearing fluid rich in ore-forming elements. When the external conditions change, under the combined action of various metallogenic mechanisms, the ore-bearing fluid precipitates in the favorable metallogenic parts such as the top of the volcanic rock and the inner and outer contact zones of the periphery, forming a Cu-Pb-Zn deposit. Some ore-bearing hydrothermal fluids continue to migrate along the fault to the farther end, forming Pb-Zn mineralization in the contact zone between sub-volcanic rocks and volcanic rocks. These sulfides are mostly disseminated and veinlet disseminated. When it encounters the geological conditions of fault structure development (mainly including the secondary fault structure of volcanic mechanism and the structural fracture zone of peripheral strata), due to the change of metallogenic physical and chemical conditions, a large number of metal elements are precipitated, forming the vertical zoning characteristics of lead and zinc in the upper part and copper in the lower part (Figure 15).

7 Conclusion

- (1) Based on the crosscutting relationship of veins, mineral assemblages, and ore textures, the mineralization process of the Chazangcuo deposit is categorized into three periods and four stages: (1) the magmatic-hydrothermal mineralization period, including quartz-pyrite-sphalerite stage I; (2) the hydrothermal mineralization period, consisting of medium-low-temperature hydrothermal sulfide stage II and chlorite-carbonate mineral stage III; (3) the supergene period, identified by supergene oxidation stage IV.
- (2) Analyses of major elements, trace elements, and REEs, alongside sulfur and lead isotopes, reveal low contents of trace elements and REEs in the samples from the Chazangcuo deposit. The Nb/Ta, Zr/Hf, and Rb/Sr ratios imply a predominantly crustal origin for the materials. The $\delta^{34}\text{S}$ values predominantly align in a tower-shape

distribution, suggesting a primary derivation from a relatively homogeneous magmatic source. The lead isotopic ratios and associated metrics suggest that the lead predominantly originates from the upper crust.

- (3) Investigations into fluid inclusions and electron probe microanalysis highlight the strong association of the Chazangcuo deposit with magmatic-hydrothermal activity, medium-low mineralization temperatures, shallow mineralization depths, and a weakly reducing metallogenic setting. These classify the Chazangcuo deposit as an epithermal low-temperature magmatic-hydrothermal type. The metallogenic model has the vertical zoning characteristics of lead-zinc in the upper part and copper in the lower part.

Data availability statement

The original contributions presented in the study are included in the article/Supplementary Material, further inquiries can be directed to the corresponding author.

Author contributions

YL: Conceptualization, Data curation, Investigation, Methodology, Software, Visualization, Writing—original draft, Writing—review and editing. JW: Data curation, Funding acquisition, Investigation, Project administration, Supervision, Writing—review and editing. ZY: Investigation, Methodology, Writing—review and editing. SW: Investigation, Methodology, Supervision, Writing—review and editing. HR: Resources, Visualization, Writing—review and editing. MM: Resources, Validation, Writing—review and editing. ZW: Investigation, Software, Writing—review and editing. JH: Visualization, Writing—review and editing.

Funding

The author(s) declare that financial support was received for the research, authorship, and/or publication of this article. This study was financially supported by the National Natural Science Foundation of China (No. 42164007).

Acknowledgments

The authors would like to extend their sincere gratitude to the reviewers for their detailed comments.

Conflict of interest

Author ZY was employed by Tibet Xinhu Mining Company Limited.

The remaining authors declare that the research was conducted in the absence of any commercial or financial relationships that could be construed as a potential conflict of interest.

Publisher's note

All claims expressed in this article are solely those of the authors and do not necessarily represent those of their affiliated

organizations, or those of the publisher, the editors and the reviewers. Any product that may be evaluated in this article, or claim that may be made by its manufacturer, is not guaranteed or endorsed by the publisher.

References

- Chen, X. F., Bai, R. L., Guo, D. B., and Liu, G. X. (2024). The occurrence of cadmium and ore genesis in the Bijishan Lead-zinc deposit: evidence from LA-ICP-MS trace elements and *in-situ* sulfur isotope of sulfide. *Geol. Bull. China*, 1–25.
- Chung, S. L., Chu, M. F., Zhang, Y. Q., Xie, Y., Lo, C. H., Lee, T. Y., et al. (2005). Tibetan tectonic evolution inferred from spatial and temporal variations in post-collisional magmatism. *Earth-Science Rev.* 68, 173–196. doi:10.1016/j.earscirev.2004.05.001
- Cook, N. J., Ciobanu, C. L., and Mao, J. (2009). Textural control on gold distribution in as-free pyrite from the dongping, huangtuliang and hougou gold deposits, north China craton (hebei province, China). *Chem. Geol.* 264 (1–4), 101–121. doi:10.1016/j.chemgeo.2009.02.020
- Dai, J. (2017). *Metallogenesis of juno porphyry Cu (Mo-Au) deposit, angren, Tibet, China*. Chengdu: Chengdu University of Technology.
- Dai, J., Ni, S. J., Huang, Y., Ding, J., and Zhou, Y. M. (2018). Genesis of rutile from metallogenic porphyry in the Zhuenuo Porphyry-type Cu-Mo deposit, Tibet, China, and its significance for prospecting. *Acta Geol. Sin.* 92 (6), 1228–1239.
- Fei, G. C., Duo, J., Wen, C. Q., Yang, Z. X., Long, X. R., and Zhou, X. (2011). S, Pb and Sr isotopic compositions for tracing sources of ore-forming materials in Dongzhongla lead-zinc deposit in Tibet. *Mineralogy Petrology* 31 (4), 52–57. doi:10.19719/j.cnki.1001-6872.2011.04.009
- Fu, Q., Huang, K. X., Zheng, Y. C., Yang, Z. S., and Duan, L. F. (2015). Ar-Ar age of muscovite from skarn orebody of the Mengya lead-zinc deposit in Tibet and its geodynamic significance. *Acta Geol. Sin.* 89 (3), 569–582. doi:10.19762/j.cnki.dizhixuebao.2015.03.011
- Gao, S. B. (2015). “Copper-iron polymetal metallogenic regularity and election of target areas in the western of Gangdise metallogenic belt,” in *Tibet*. Wuhan: China University of Geosciences.
- Ge, Z. L., Gu, X. X., Zhang, Y. M., Zheng, Y. R., Liu, M., Hao, D., et al. (2023). Mineralogical characteristics and metallogenic indication of gold-bearing sulfides in the Jinpenliang gold deposit, Zhushui-Shanyang ore cluster area, South Qinling. *Northwest. Geol.* 56 (5), 278–293. doi:10.12401/j.nwg.2023118
- Gong, X. J., Yang, Z. S., Zhuang, L. L., and Ma, W. (2019). Genesis of Narusongduo Pb-Zn deposit, Tibet: constraint from *in-situ* LA-ICP-MS analyses of minor and trace elements in sphalerite. *Mineral. Deposits* 38 (6), 1365–1378. doi:10.12097/j.issn.1671-2552.2022.11.002
- Gong, X. J., Yang, Z. S., Zhuang, L. L., and Ma, W. (2022). *In situ* zircon Hf-O isotopic characteristics and petrogenesis of Late Cretaceous quartz diorite in the Narusongduo Pb-Zn mining area, Tibet. *Geol. Bull. China* 41 (11), 1915–1926. doi:10.16111/j.0258-7106.2019.06.011
- Green, T. H. (1995). Significance of Nb/Ta as an indicator of geochemical processes in the crust-mantle system. *Chem. Geol.* 120 (3), 347–359. doi:10.1016/0009-2541(94)00145-x
- He, L. F., Di, Q. Y., Wang, Z. X., Lai, J. Q., Xue, G. Q., and Guo, W. B. (2023). Crustal structures of the Qimantagh metallogenic belt in the Northern Tibetan Plateau from magnetotelluric data and their correlation to the distribution of mineral deposits. *Minerals* 13 (2), 225. doi:10.3390/MIN13020225
- Hofmann, A. W. (1988). Chemical differentiation of the Earth: the relationship between mantle, continental crust, and oceanic crust. *Earth Planet. Sci. Lett.* 90 (3), 297–314. doi:10.1016/0012-821x(88)90132-x
- Hou, Z. Q., Mo, X. X., Yang, Z. M., Wang, A. J., Pan, G. T., Qu, X. M., et al. (2006a). Metallogenesis in the collisional orogen of the Qinghai-Tibet Plateau: tectonic setting, tempo-spatial distribution and ore deposit types. *Geol. China* 33 (2), 340–351.
- Hou, Z. Q., Zeng, P. S., Gao, Y. F., Du, A. D., and Fu, D. M. (2006b). The Himalayan Cu-Mo-Au mineralization in the eastern Indo-Asian collision zone: constraints from Re-Os dating of molybdenite. *Miner. Deposita* 22, 177–199.
- Hou, Z. Q., Zheng, Y. C., Yang, Z. M., and Yang, Z. S. (2012). Metallogenesis of continental collision setting: Part I. Gangdise Cenozoic porphyry Cu-Mo systems in Tibet. *Mineral. Deposits* 31 (4), 647–670. doi:10.16111/j.0258-7106.2012.04.002
- Jiang, J. S. (2018). *Genesis of polymetallic deposits and prospecting potential in the Linzong area, western gangdise belt, Tibet*. Wuhan: China University of Geosciences.
- Jiang, J. S., Zheng, Y. Y., Gao, S. B., Xu, J., Tian, K., Huang, L. L., et al. (2015). Geochemistry genesis of Chazangcuo Cu-Pb-Zn deposit, Tibet: constraints from C-H-O-S-Pb isotope. *Earth Sci.* 40 (6), 1006–1016. doi:10.3799/dqkx.2015.084
- Ke, X. Z., Long, W. G., Zhou, D., Wang, J., and Zhong, S. Y. (2017). Metallogenesis of the main collisional period in mid-western Gangdise: zircon U-Pb geochronology of the granite porphyry in Dexin deposit, Tibet. *Geol. Bull. China* 36 (5), 772–779.
- Ke, X. Z., Wang, J., Zhong, S. Y., and Gao, X. (2019). Sulfur and lead isotope composition of hydrothermal vein type lead-zinc deposits in Zexue area, Tibet and its implications for the origin of ore-forming materials. *Geol. China* 46 (3), 629–641. doi:10.12029/gc20190313
- Kong, D. X., Xu, J. F., Yin, J. W., Chen, J. L., Li, J., Guo, Y., et al. (2015). Electron microprobe analyses of ore minerals and H-O, S isotope geochemistry of the Yuerya gold deposit, eastern Hebei, China: implications for ore genesis and mineralization. *Ore Geol. Rev.* 69, 199–216. doi:10.1016/j.oregeorev.2015.01.020
- Li, C., Zhai, Q. G., Xu, F., and Zhu, Z. Y. (2005). Kinematics of the active north-south-trending chazang Co-XainzaTectonic belt, xizang (Tibet). *Geol. Rev.* 51 (4), 353–359. doi:10.16509/j.georeview.2005.04.001
- Li, G. M., Zhang, L. K., Zhang, Z., Xia, X. B., Liang, W., and Hou, C. Q. (2021). New exploration progresses, resource potentials and prospecting targets of strategic minerals in the southern Qinghai-Tibet Plateau. *Sediment. Geol. Tethyan Geol.* 41 (2), 351–360. doi:10.19826/j.cnki.1009-3850.2021.03012
- Li, J. L., Zhang, Y. M., Gu, X. X., Meng, F. J., Gao, H. J., and Wang, L. (2017). Geological characteristics of sulfides of the Xiyi MVT-type Pb-Zn Ore deposit in Yunnan and EPMA analysis of the sulfides. *Geol. Explor.* 53 (1), 23–34. doi:10.13712/j.cnki.dzykt.2017.01.004
- Li, W. Z., Yuan, G. L., Song, S. C., Xie, H. L., Song, W. G., Gong, Z. Y., et al. (2019). Geological characteristics and electron probe analysis of sulfides in the Xialugou Cu-Pb-Zn deposit of Qinghai Province. *Geol. Explor.* 55 (2), 447–460. doi:10.12134/j.dzykt.2019.02.001
- Li, X. D., Zhang, Y., Han, R. S., Wang, L., Wu, J. B., and Cheng, G. (2022). Research progress of fluid inclusions and its application in ore deposit. *Geol. Rev.* 68 (6), 2305–2318. doi:10.16509/j.georeview.2022.07.065
- Li, Y. S., Lv, Z. C., Yan, G. S., Zhen, S. M., and Du, Z. Z. (2012). Isotopic characteristics of S, Pb, H and O of Jiama copper-polymetallic ore deposit, Tibet and their significance. *Earth Sci. Front.* 19 (4), 72–81.
- Liang, X. F., Chen, L., Tian, X. B., Chu, Y., and Li, W. T. (2023). Uplifting mechanism of the Tibetan Plateau inferred from the characteristics of crustal structures. *Sci. China Earth Sci.* 66 (12), 2770–2790. doi:10.1007/s11430-023-1158-5
- Liu, Y., Cook, N. J., Ciobanu, C. L., Liu, Y. P., Zhang, Q., Liu, T. G., et al. (2011). Trace and minor elements in sphalerite from base metal deposits in South China: a LA-ICPMS study. *Ore Geol. Rev.* 39 (4), 188–217. doi:10.1016/j.oregeorev.2011.03.001
- Ling, C., Li, G. M., Zhang, Z., Zhang, L. K., and Cao, H. W. (2021). Source of metallogenic material of Lawu Zn-Cu polymetallic deposit in Gangdise metallogenic belt, Tibet:sulfide LA-MC-ICP-MS *in situ* S isotope constraint. *Northwest. Geol.* 54 (2), 43–54. doi:10.19751/j.cnki.61-1149/p.2021.02.004
- Liu, B. (2001). Density and Isochoric formulae for NaCl-H₂O inclusions with medium and high salinity and their applications. *Geol. Rev.* (6), 617–622. doi:10.16509/j.georeview.2001.06.015
- Liu, B., and Duan, G. X. (1987). The density and isochoric formulae for NaCl-H₂O fluid inclusions (salinity≤25 Wt%) and their applications. *Acta Mineral. Sin.* (4), 345–352. doi:10.16461/j.cnki.1000-4734.1987.04.011
- Liu, T. T., Tang, J. X., Liu, H. F., Zhang, J. S., Cui, X. L., and Gao, Y. M. (2011). Sulfur and lead isotope composition and tracing for sources of ore-forming materials in the Dongzhongla Pb-Zn deposits in Mozhuogongka County, Tibet. *Geoscience* 25 (5), 869–876.
- Mo, X. X., Dong, G. C., Zhao, Z. D., Guo, T. Y., Wang, L. L., and Chen, T. (2005). Timing of magma mixing in the Gangdise magmatic belt during the India-Asia collision, Zircon SHRIMP U-Pb dating. *Acta Geol. Sin.* 79, 66–76. doi:10.1111/j.1755-6724.2005.tb00868.x
- Ni, P., Fan, H. R., Pan, J. Y., Chi, Z., and Cui, J. M. (2021). Progress and prospect of fluid inclusion research in the Past Decade in China (2011–2020). *Bull. Mineralogy, Petrology Geochem.* 40 (4), 802–818. doi:10.19658/j.issn.1007-2802.2021.40.056
- Ohmoto, H. (1972). Systematics of sulfur and carbon isotopes in hydrothermal ore deposits. *Econ. Geol.* 67 (5), 551–578. doi:10.2113/gsecongeo.67.5.551
- Ohmoto, H. (1986). Stable isotope geochemistry of ore deposits. *Rev. Mineralogy Geochem.* 16 (1), 491–559.

- Pivetta, C. P., Benedini, L., Marcos, P., Cocola, M., Barros, M. V., Gregori, D., et al. (2024). Characterization of arroyo verde epithermal deposit: paragenesis, mineral geochemistry, geochronology and fluid inclusions in lower chon aike volcanism, Argentina. *J. Earth Sci.* 35, 62–84. doi:10.1007/s12583-023-1823-5
- Ren, W. Q., Wang, L., Guan, S. J., Xu, J. J., He, H., and Zhu, E. Y. (2023). Genesis and fluid evolution of the Hongqiling Sn-W polymetallic deposit in Hunan, South China: constraints from geology, fluid inclusion, and stable isotopes. *Minerals* 13 (3), 395. doi:10.3390/min13030395
- Rudnick, R. L., and Fountain, D. M. (1995). Nature and composition of the continental crust: a lower crustal perspective. *Rev. Geophys.* 33 (3), 267–309. doi:10.1029/95RG01302
- Sakai, H. (1968). Isotopic properties of sulfur compounds in hydrothermal processes. *Geochem. J.* 2 (1), 29–49. doi:10.2343/geochemj.2.29
- Schwartz, M. O. (2000). Cadmium in zinc deposits: economic geology of a polluting element. *Int. Geol. Rev.* 42 (5), 445–469. doi:10.1080/00206810009465091
- Seal, R. R. (2006). Sulfur isotope geochemistry of sulfide minerals. *Rev. Mineralogy Geochem.* 61 (1), 633–677. doi:10.2138/rmg.2006.61.12
- Shen, J. F., Li, S. R., Huang, S. F., Qing, M., Zhang, H. F., and Xu, B. (2021). The decenary new advances on the genetic mineralogy and prospecting mineralogy (2010–2020). *Bull. Mineralogy, Petrology Geochem.* 40 (3), 610–623+777. doi:10.19658/j.issn.1007-2802.2021.40.036
- Song, Y., Tang, J. X., Qu, X. M., and Wang, D. H. (2014). The generalized concept and metallogenic characteristics of Bangong Lake–Nujiang metallogenic belt in Tibet. *Mineral. Deposits* 33 (s1), 815–816. doi:10.16111/j.0258-7106.2014.s1.410
- Sun, S. S., and McDonough, W. F. (1989). Chemical and isotopic systematics of oceanic basalts: implications for mantle composition and processes. *Geol. Soc.* 42 (1), 313–345. doi:10.1144/GSL.SP.1989.042.01.19
- Sun, Y. G., Li, B. L., Sun, F. Y., Dong, J. L., Qian, Y., Yao, Z., et al. (2020). Genesis of M9 ore body of Basihu Pb–Zn deposit in Qinghai Province: constraints of fluid inclusions and H–O–S isotopic evidences. *J. Jilin Univ. Earth Sci. Ed.* 50 (5), 1373–1386. doi:10.13278/j.cnki.jjuese.20190276
- Tang, J. X. (2019). Mineral resources base investigation and research status of the Tibet Plateau and its adjacent major metallogenic belts. *Acta Petrol. Sin.* 35 (3), 617–624. doi:10.18654/1000-0569/2019.03.01
- Taylor, S. R., and McLennan, S. M. (1995). The geochemical evolution of the continental crust. *Rev. Geophys.* 33 (2), 241–265. doi:10.1029/95rg00262
- Tian, J., and Yang, G. S. (2022). Trace element characteristics of sphalerite from Dulong Tin-polymetallic deposit in Southeast Yunnan and their geological significances. *Geotect. Metallogenia* 46 (6), 1148–1166. doi:10.16539/j.ddgzyckx.2022.06.007
- Wang, L. Q., Lin, X., Li, Z., Zhang, Z., Kang, H. R., and Li, H. F. (2014). Geochronology, geochemistry and Hf isotopic compositions of the granite porphyry in the Mengya Pb–Zn deposit, Tibet. *Acta Geol. Sin.* 88 (12), 2572–2583. doi:10.19762/j.cnki.dizhixuebao.2014.12.029
- Wang, Q. F., Deng, J., Weng, W. J., Li, H. J., Wang, X., and Li, G. J. (2020). Cenozoic orogenic gold system in Tibet. *Acta Petrol. Sin.* 36 (5), 1315–1354. doi:10.18654/1000-0569/2020.05.02
- Wang, R., Zhang, J. B., Luo, C. H., Zhou, Q. S., Xia, W. J., and Zhao, Y. (2024). Deep process and lithospheric architectural control of Cu–REE mineralization in continental collisionzone: insights from a case study of the Gangdese and Sanjiang collisional belts. *Earth Sci. Front.* 31 (1), 211–225. doi:10.13745/j.esf.sf.2023.12.19
- Wen, D. R., Liu, D. Y., Chung, S. L., Chu, M. F., Ji, J., Zhang, Q., et al. (2008). Zircon SHRIMP U–Pb ages of the Gangdese batholith and implications for neotethyan subduction in southern Tibet. *Chem. Geol.* 252, 191–201. doi:10.1016/j.chemgeo.2008.03.003
- Wu, D. H., Pan, J. Y., Xia, F., Huang, G. W., and Lai, J. (2019). The mineral chemistry of chlorites and its relationship with uranium mineralization from Huangsha uranium mining area in the middle Nanling range, SE China. *Minerals* 9 (3), 199. doi:10.3390/min9030199
- Wu, K. X., Hu, R. Z., Bi, X. W., Peng, J. T., and Tang, Q. L. (2002). Ore lead isotopes as a tracer for ore-forming material sources: a review. *Earth Environ.* 30 (3), 73–81.
- Wu, W., He, R. Z., Ji, Z. B., Niu, X., Wang, C., and Li, Z. X. (2023). Crustal structure and mineralization indications of the Jiama–Qulong deposits. *Acta Geol. Sin.* 97 (8), 2534–2546. doi:10.19762/j.cnki.dizhixuebao.2023120
- Xiao, R. G., Liu, J. D., Fei, H. C., Liu, J., Yuan, Z. L., Wang, C. Z., et al. (2008). *Geochemistry on rock and mineral deposit*. Beijing: Seismological Press, 288–292.
- Xie, F. W., Lang, X. H., Tang, J. X., He, Q., Deng, Y. L., Wang, X. H., et al. (2022). Metallogenic regularity of Gangdese metallogenic belt, Tibet. *Mineral. Deposits* 41 (5), 952–974. doi:10.16111/j.0258-7106.2022.05.005
- Xiong, Y., Tang, J. X., Tang, P., Lin, B., Tang, X. Q., Sun, M., et al. (2022). Mineralogical characteristics and geological significance of sphalerite from Jiama porphyry metallogenic system, Tibet. *Mineral. Deposits* 41 (6), 1164–1181. doi:10.16111/j.0258-7106.2022.06.005
- Xu, B., Hou, Z. Q., Griffin, W. L., O'Reilly, S. Y., Zheng, Y. C., Wang, T., et al. (2022). *In-situ* mineralogical interpretation of the mantle geophysical signature of the Gangdese Cu–porphyry mineral system. *Gondwana Res.* 111, 53–63. doi:10.1016/j.gr.2022.07.005
- Yang, Y., Luo, T. Y., Huang, Z. L., Yang, Z. S., Tian, S. H., and Qian, Z. K. (2010). Sulfur and lead isotope compositions of the Narusongduo Silver–Zinc–Lead deposit in Tibet: implications for the sources of plutons and metals in the deposit. *Acta Mineral. Sin.* 30 (3), 311–318. doi:10.16461/j.cnki.1000-4734.2010.03.005
- Yao, X. F., Tang, J. X., Ding, S., Zheng, W. B., Zhang, W. Y., and Shan, L. (2014). Genesis and main differences of Jiama and Qulong super-large deposit in Gangdese metallogenic belt. *Acta Geol. Sinica-English Ed.* 88 (s2), 633–634. doi:10.1111/1755-6724.12374_64
- Yu, Y. S. (2011). *Mineralization of skarn Fe–Cu deposits in nixiong orefield, coqen, Tibet*. Beijing: Chinese Academy of Geological Sciences.
- Zartman, R. E., and Doe, B. R. (1981). Plumbotectonics—the model. *Tectonophysics* 75 (1–2), 135–162. doi:10.1016/0040-1951(81)90213-4
- Zhang, C. Q., Li, H. M., Dai, J. Z., Yang, X. Z., Li, L., Mao, J. W., et al. (2006). Lead isotope research on lead–zinc deposits. *Mineral. Deposits* 25 (s1), 213–216. doi:10.16111/0258-7106.2006.s1.056
- Zhang, H. S., Li, Y. G., Quan, S. C., Hong, J., Sun, C., Li, J. X., et al. (2018). Geochemical characteristics of metallic sulfides from the Kaladaban deposit in Xinjiang and its implications for Pb–Zn ore-forming mechanism. *Acta Petrol. Sin.* 34 (8), 2295–2311.
- Zhang, Y. C., Zheng, Y. Y., Gao, S. B., Jiang, J. S., Tian, K., Wu, D. H., et al. (2018). H–O–S–Pb isotopic compositions of the Chagele Pb–Zn–Cu–Mo deposit, Tibet: implications for the ore-forming processes and comparison with Pb–Zn (Cu–Mo) deposits in middle-east segment of the nyaingentanglha metallogenic belt. *Geotect. Metallogenia* 42 (3), 467–479. doi:10.16539/j.ddgzyckx.2018.03.005
- Zheng, W., Chen, M. H., Zhao, H. J., Hao, H. D., Chang, L. Z., Hu, Y. G., et al. (2012). Characteristics of sulfides and S–Pb isotope composition in the Tiantang Cu–Pb–Zn polymetallic deposit of Guangdong Province and their Geological implications. *Geol. China* 39 (6), 1830–1846.
- Zheng, Y. F., Xu, B. L., and Zhou, G. T. (2000). Geochemical studies of stable isotopes in minerals. *Earth Sci. Front.* (2), 299–320.
- Zhu, B. Q., Li, X. H., Dai, T. M., Chen, Y. W., Fan, S. K., Gui, X. T., et al. (1998). *Theory and application of isotopic system in earth science—also on the slow evolution of the continental crust of China*. Beijing: Science Press.
- Zhu, D. C., Mo, X. X., Zhao, Z. D., Niu, Y. L., Pan, G. T., Wang, L. Q., et al. (2009). Permian and early cretaceous tectonic magmatism in southern Tibet and tethyan evolution: new perspective. *Earth Sci. Front.* 16 (2), 1–20.
- Zhu, D. C., Zhao, Z. D., Niu, Y. L., Mo, X. X., Chung, S. L., Hou, Z. Q., et al. (2011). The Lhasa Terrane: record of a microcontinent and its histories of drift and growth. *Earth Planet. Sci. Lett.* 301 (1–2), 241–255. doi:10.1016/j.epsl.2010.11.005